SLAC-PUB-5783
March 1992
(A)

THE TRANSVERSE WAKEFIELD OF A DETUNED X-BAND ACCELERATOR STRUCTURE*

KARL L.F. BANE

Stanford Linear Accelerator Center
Stanford University, Stanford, California 94309

and

ROBERT L. GLUCKSTERN

Physics Department
University of Maryland, College Park, Maryland 20742

(Submitted to Particle Accelerators)

* Work supported by the US Department of Energy, contract DE – AC03 – 76SF00515.

Abstract

In the design of future electron/positron colliders in the TeV region with high luminosities, the transverse wakefields generated by one bunch in a train of accelerated bunches may deflect one or more of the subsequent bunches. In this paper we analyze the mode structure and the transverse wakefields in a tapered cavity, including the effect of coupling between adjacent cells. The parameters of the equivalent circuit chain used in the analysis are obtained from computer runs for periodic structures corresponding to different cells of the cavity. Following the guidelines suggested by an analysis of Maxwell's equations for one or two deflecting bands we obtain numerical solutions for the wakefields for different patterns of detuning. We find that Gaussian detuning of the geometric cell parameters within a cavity dramatically decreases the wakefields obtained with linear detuning. Several examples of mode structure, mode frequency distribution, kick factors, and wakefields are presented, confirming this conclusion.

1. Introduction

1.1 Introduction

Experience with the Stanford Linear Collider (SLC) has encouraged consideration of future electron/positron colliders in the TeV region as a vehicle for exploring the structure of matter at extremely high energies and luminosities. Design efforts are currently under way at many laboratories.[1] Many of these designs involve the acceleration of trains of bunches. Among the technical problems with such an idea is that one bunch beam in the train is capable of exciting transverse wakefields of the accelerator cavities which, in turn, will deflect following beam bunches and result in emittance growth. Two methods for curing this problem are to damp the transverse modes of the cavity[2] or to detune them.[3] In this paper we will study the detuning of the modes.

The wakefield of an accelerator cavity is given by a sum over its normal modes. Detuning can cause the terms in this sum to add in such a way that the wakefield

is greatly reduced over some finite range. Detuning can therefore be especially effective in a design, such as that of the Next Linear Collider (NLC),[4] in which there are only a few bunches in a relatively short train. The proposed, detuned NLC cavity is a disk-loaded, accelerator structure composed of approximately of 200 cells, operating at X-band, at 11.42 GHz. The most troublesome transverse modes of the cavity are those belonging to the first dipole passband, with frequencies near 15 GHz, and, in this paper, these are the modes upon which we will focus. Detuning of these modes is accomplished by varying the cell dimensions gradually from one end of the cavity to the other. A special feature of the detuned NLC cavity is that the cell-to-cell coupling of the modes changes sign somewhere in the middle of the structure.

In the NLC the proposed mode of operation is to accelerate bunches in trains of 10, with a bunch spacing (within each train) of 42 cm. Simulations have found, for the parameters of the NLC, that the transverse wakefield at the positions of the nine trailing bunches needs to be kept at or below 1 $MV/nC/m^2$ in order to avoid emittance growth.[5] Earlier, approximate calculations of the wakefields, which did not include the cell-to-cell coupling of the modes, have shown that by choosing the cell frequencies according to the proper Gaussian distribution, the above level of cancellation can be achieved.[3,6] A specific goal of this report is to see if this conclusion still holds when the cell-to-cell coupling is included in the calculation.

Our approach to the problem is to first find the modes of the detuned NLC cavity, and then to find the wakefield. Our cavity has about 200 cell, each with slightly different dimensions. It appears that finding the modes of such a structure directly, by solving Maxwell's equations, is beyond the capabilities of present day computers. Therefore, in this paper, we will model the detuned cavity by a chain of coupled resonant circuits, with each loop of the chain representing one cavity cell. We obtain the modes of the circuit by solving a matrix eigenvalue problem. The solution of this problem gives us the frequencies, kick factors, and quality factors of the normal modes of the cavity which, in turn, give us the wakefield. The advantage of first finding the normal modes of the circuit rather than performing a

direct time domain integration of the currents in the circuit is that in this way one calculation gives us the wakefield for all distances. In the second part of this report we repeat the process using a double band of infinite circuits to model the cavity, a model that we derive from the properties of Maxwell's equations at an iris, which duplicates the dispersion curves of the lowest two bands more accurately.

Equivalent circuits have been used often to model rf cavities. Early examples describing their use for finding the normal modes of a multi-cell cavity are papers by T. Smith[7] and by D. Nagle, *et.al.*[8] J. Rees[9] used this approach to calculate detuning in the PEP five-cell rf cavities. All three papers used largely analytical techniques, using perturbation theory for finding the effects of detuning. As in the work of J. Rees, our single circuit chain couples through mutual inductors. More recently M. Drevlak[10] applied equivalent circuits that couple through inductors or capacitors to the SLAC linear accelerator cavity to numerically find the modes and the wakefields. His circuit models are applicable to structures for which the coupling does not change sign within the cavity. K. Bane and N. Holtkamp[11] using a more complicated circuit, solve a non-linear eigenvalue problem, to find modes of the NLC detuned cavity. A preliminary version of the present work was presented by R. Miller at Protvino in September 1991.[12] Finally Yamamoto, *et.al.*,[13] apply direct time domain integration of the circuits to find the wakefield of the JLC detuned cavity (which is very similar to the NLC cavity), confirming the results presented here.

1.2 Dispersion Curves

The cavities under consideration for the NLC are disk-loaded structures with fundamental frequency 11.424 GHz operating in the $2\pi/3$ mode. The cell geometry, as we will approximate it in this report, is sketched in Fig. 1. (The real geometry will have rounded irises and likely pumping slots.) The four parameters are iris radius a, waveguide radius b, iris thickness t (nominally set to 1.46 mm), and period L (fixed at 8.75 mm). The parameters a and b vary from cell to cell in such a way

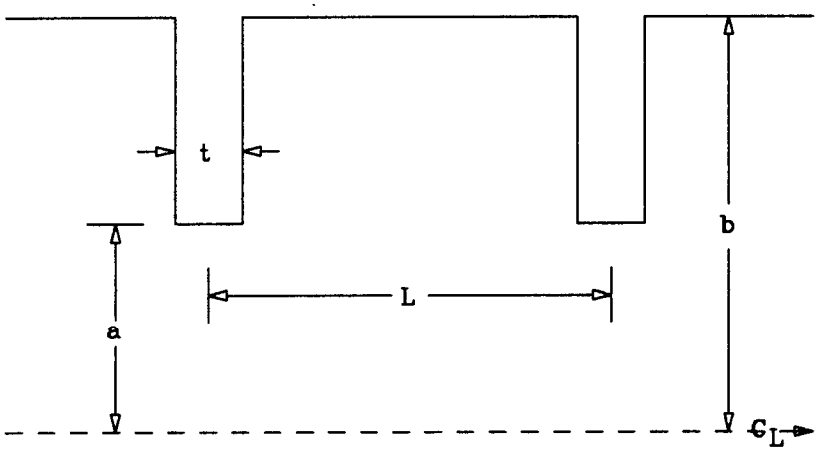

Fig. 1. The cell geometry that we consider in this paper.

so as to detune the dipole mode frequency while keeping the fundamental mode frequency fixed.

In order to understand the mode spectrum of the deflecting modes in such a structure, we use the computer program TRANSVRS.[14] This program calculates the frequencies and kick factors for an infinitely periodic structure composed of the type of cells shown in Fig. 1. In Fig. 2 we display the lowest two dispersion bands, as calculated by TRANSVRS, for a periodic structure whose parameters are chosen to match three typical cells in our detuned structure. In this figure we plot the frequency ν against the phase advance per cell ϕ. The curves labeled C, D, and E represent respectively the parameters of a cell near the front, middle, and end of the detuned structure. The cell dimensions of these structures are given in Table 1. The dotted line in Fig. 2 displays the speed of light line. We note that the speed of light line crosses the lower dipole band of the three structures near pi phase advance.

From the figure we note that the lower band, which appears to be the more important in deflecting the beam, has the usual cosine-like shape, except for the fact that it goes from forward to backward wave as one goes from the first cell to the last. At first we shall take as our model a single coupled circuit chain, with a coupling constant which varies from positive to negative, and a resonant frequency

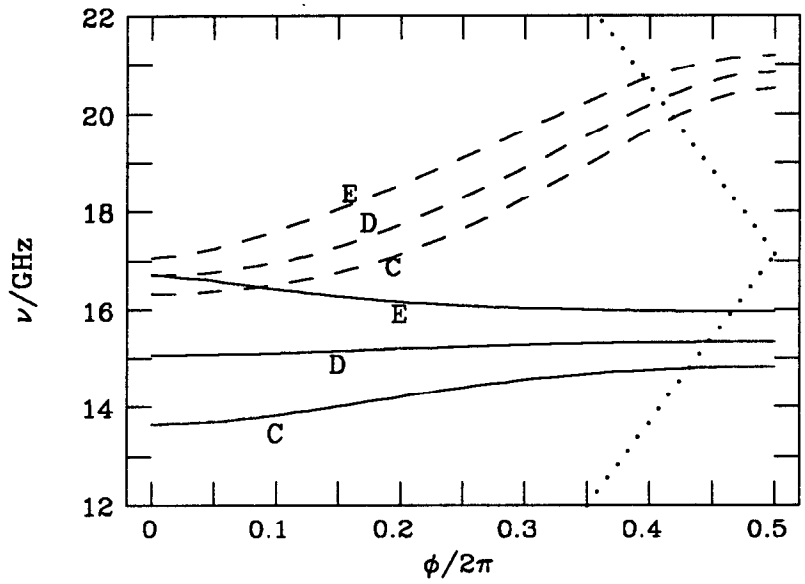

Fig. 2. The first two dipole bands of a periodic structure with the dimensions of cells C, D, and E. The dots give the speed of light line.

Table 1. Seven combinations of iris radius a and cavity radius b in a periodic, disk-loaded structure for which the fundamental frequency is 11.429 GHz. In all cases the period $L = 8.75$ mm and the iris thickness $t = 1.46$ mm. Also given are some properties of the first dipole band: the synchronous frequency ν_s, the kick factor K_s, and the resonator frequency ν_m and relative coupling factor η (to be discussed in Chapter 2).

Label	a (mm)	b (mm)	ν_s (GHz)	K_s (MV/nC/m^2)	ν_m (GHz)	η
A	6.500	11.80	13.95	17.1	12.60	+.202
B	5.875	11.44	14.34	23.0	13.35	+.142
C	5.250	11.12	14.80	31.0	14.21	+.081
D	4.625	10.83	15.34	41.6	15.21	+.018
E	4.000	10.58	15.97	54.4	16.33	−.046
F	3.375	10.39	16.65	68.5	17.01	−.044
G	2.750	10.24	17.29	80.1	17.49	−.023

which increases as one goes from the first cell to the last. This model is only approximate, however. In Fig. 3 we plot again the dispersion curves of Fig. 2, but now as ν^{-2} against $\cos\phi$. We shall see in Chapter 2 that a single coupled circuit model corresponding to magnetic coupling between cells gives a linear variation of ν^{-2} *vs* $\cos\phi$, which does not agree with the behavior of the upper curves in Fig. 3 (corresponding to the lower curves in Fig. 2). In Chapter 3, we shall derive a double chain of coupled circuits to more exactly duplicate the curves in Figs. 2 and 3, but the mode spectrum for the tapered cavity will be seen as not changing a great deal from that obtained with the single chain.

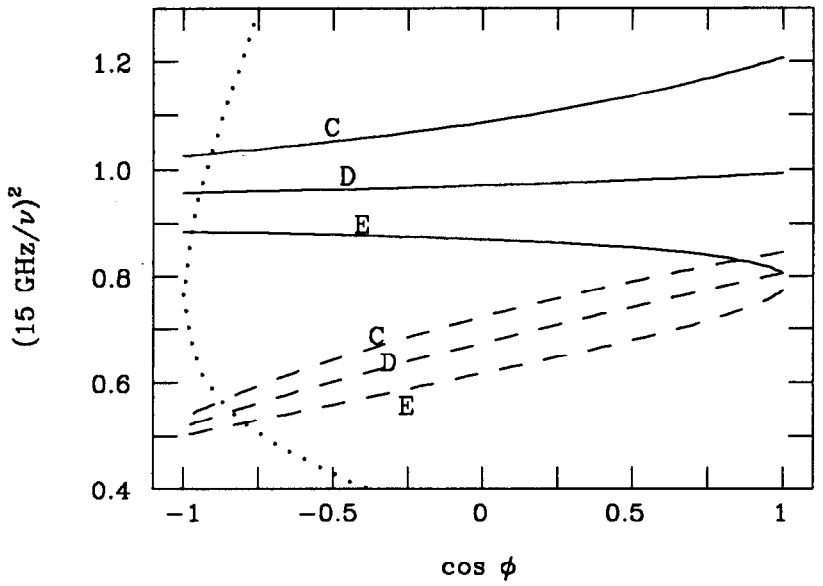

Fig. 3. The dispersion curves of Fig. 2 but plotted as ν^{-2} *vs* $\cos\phi$. The dots give the speed of light curve.

1.3 The Transverse Wakefield of a Detuned Structure

We begin by briefly discussing some important properties of the wakefield $W(s)$ of a structure. (For a more thorough discussion of wakefields see, for example, Ref. 15.) Consider a point particle with charge q_e moving parallel to the axis of a closed, cylindrically symmetric structure at offset x_e (which is near the axis) and

with velocity c. A test particle which moves at offset x (near or on the axis) and at velocity c, but at a distance s behind the leading charge, will gain in the x direction the voltage $x_e q_e W(s)$ per meter of travel. The dipole wakefield of the structure $W(s)$ is given by

$$W(s) = 2\sum_n K_n \sin\frac{2\pi\nu_n s}{c}\, e^{-\pi\nu_n s/(cQ_n)} \qquad s > 0, \tag{1.1}$$

with K_n the kick factor, ν_n the frequency, and Q_n the quality factor of the n^{th} dipole mode of the structure. The units of the wakefield will be given as MV/nC/m^2. Note that once we know the frequencies, the kick factors, and the quality factors of the modes of a cavity we know the wakefield for all s. In this paper we will normally assume that the Q's of the modes are sufficiently high so that (for our purposes) the damping terms in Eq. (1.1) can be set to 1. (For completeness, however, we will discuss briefly the damping of the modes in Secs. 2.4 and 2.5.1.) Note that the dipole modes also interact longitudinally with the beam. The longitudinal dipole voltage is given by $-x_e x q_e W_z(s)$ and the longitudinal dipole wakefield by $W_z(s) = 2\sum_n \mathcal{K}_n \cos(2\pi\nu_n s/c)$, with the dipole mode loss factors given by $\mathcal{K}_n = 2\pi\nu_n K_n/c$.

Eq. (1.1) gives also the wakefield of a periodic structure as long as we interpret K_n and ν_n as the kick factor and the frequency of the *synchronous* modes of the structure. (To differentiate this case we use the symbols K_{sn} and ν_{sn}.) For a periodic structure with NLC type parameters we find from TRANSVRS that the kick factor of the first dipole band is an order of magnitude larger than for any of the higher bands. After a distance s large compared to the wavelength of this mode the higher modes will have gotten out of phase with each other and the wake will be well approximated by the first mode alone. Since in this paper we are only interested in the bunch-to-bunch wake forces, and since the bunches are separated by many wavelengths, we are in this large s regime; therefore throughout this paper we will include only the effects of the first (or at most the first two) dipole bands of the structure.

A detuned cavity consists of many cells with the cell geometry varying gradually as we move along the structure. For such a structure the wakefield can be divided into two qualitatively distinct regions: into a short range region for which the wake can be described by the average properties of the kick factor and the spectrum of the modes, and a long range region for which the wake depends on the spacing of the individual modes. Over the first region, *i.e.* for s not too large, we can approximate the sum of Eq. (1.1) by the integral

$$W(s) \approx 2 \int_{-\infty}^{\infty} d\nu \, K \frac{dn}{d\nu} \sin \frac{2\pi\nu s}{c} \quad , \tag{1.2}$$

with K the kick factor and $dn/d\nu$ the distribution of frequencies, both of which are continuous functions of ν. Suppose that $K\, dn/d\nu$ is a narrow function centered about $\bar{\nu}$, as will be the case for our detuned structure. Then Eq. (1.2) can be conveniently written as

$$W(s) \approx 2\Im\mathrm{m} \left[e^{2\pi i\bar{\nu}s/c} \int_{-\infty}^{\infty} dx \, K(x+\bar{\nu}) \frac{dn}{d\nu}(x+\bar{\nu}) e^{2\pi i x s/c} \right] \quad , \tag{1.3}$$

with $\Im\mathrm{m}$ signifying the imaginary part of the argument. We see that the wake consists of a rapidly varying part, oscillating at frequency $\bar{\nu}$, and a slowly varying part (the envelope) that is given by the Fourier transform of the function $K\, dn/d\nu$ after it has been centered about zero. If the frequency distribution is uniform with full frequency spread $\Delta\nu$ then the wakefield is approximately given by

$$W(s) \approx 2\bar{K} \sin \frac{2\pi\bar{\nu}s}{c} \cdot \frac{\sin(\pi s \Delta\nu/c)}{(\pi s \Delta\nu/c)} \quad , \tag{1.4}$$

with $\bar{K}$ the average value of K. If the frequency distribution is Gaussian, with rms width σ_ν, then

$$W(s) \approx 2\bar{K} \sin \frac{2\pi\bar{\nu}s}{c} e^{-2(\pi\sigma_\nu s/c)^2} \quad . \tag{1.5}$$

In this case the envelope drops also as a Gaussian. It seems reasonable to expect that the proper Gaussian frequency distribution is near ideal in the sense of giving

a rapid drop in the wakefield for a given total frequency spread, and this is the motivation for choosing Gaussian detuning. Finally we should emphasize that over the second, longer range region of the wakefield, the above, continuous analysis is no longer valid. More precisely, for $s \sim c/\delta\nu$, with $\delta\nu$ the typical spacing of the modes, the wakefield envelope will no longer be determined by $K\, dn/d\nu$. In this regime even for a Gaussian distribution the contribution of the individual modes will no longer cancel well.

1.4 The Uncoupled Calculation of the Wakefield

In this section we review briefly the method that to date has been used to obtain the wakefield of a detuned version of the NLC accelerator structure.[3] It is a calculation which does not properly include the effects of coupling between neighboring cells. For lack of a better label we call it the *uncoupled* solution.* We then apply this method to the NLC parameters and present the results. Throughout the rest of this paper these results will be compared with those of more accurate calculations that do not ignore the cell-to-cell coupling.

A linear accelerator cavity of the type we consider consists of many cells that are connected, and couple, through irises to their neighbors. The wakefield of such a structure can be divided roughly into two regions in the following way: one, a short range (small s) region over which the cell-to-cell coupling does not affect the wakefield, and another, larger s region over which the coupling does affect the result. The uncoupled calculation is meant to apply only to the first of these two regions. According to this calculation the wakefield of an N-cell detuned structure is approximated by

$$W(s) = \frac{2}{N} \sum_{m}^{N} K_{s1}^{(m)} \sin \frac{2\pi \nu_{s1}^{(m)} s}{c} \quad . \tag{1.6}$$

* This solution should not be confused with what one would obtain from the resonator models, described in the following chapters, by setting all couplings to zero.

In Eq. (1.6) $K_{s1}^{(m)}$ and $\nu_{s1}^{(m)}$ represent the kick factor and frequency of the synchronous component of the first dipole mode for a periodic structure with the dimensions of cell m. (The parameters K_{s1} and ν_{s1} for several possible NLC cell geometries are given in Table 1. In this table, as elsewhere in this paper, the subscript 1 may be dropped when it is understood from the context.) How can we justify Eq. (1.6)? If the structure is composed of many cells, if the tapering is gradual, and if $2\pi\nu_s a/c$ is not very large (in our case it is on the order of 1), then we can expect that the wakefield locally can be described by the synchronous frequency and the associated kick factor of a periodic structure with the local cell geometry. And, consequently, we expect that Eq. (1.6) correctly gives the wakefield for sufficiently small s. [However, we should not be tempted to infer from Eq. (1.6) that the normal mode frequencies of the structure can be approximated by the $\nu_s^{(m)}$.] What are the limits of validity of this method? For what values of s will we need to find the coupled modes of the structure in order to obtain the correct wakefield? We can get a rough idea of the answer to this question from the dispersion curve for a typical cell geometry. A conservative estimate of the limit of validity is that it is roughly given by $s \sim 3cL/v_g$, with L the cell length and v_g the highest group velocity of the modes for the typical cell geometry.

As a numerical example of the uncoupled calculation let us take parameters appropriate for the NLC. Let us consider a structure with $N = 200$ cells and take as central frequency $\bar{\nu}_s = 15.25$ GHz. If we take a Gaussian distribution in frequencies, with $\sigma_{\nu_s}/\bar{\nu}_s = 2.5\%$, then according to Eq. (1.5) we expect the wakefield envelope to be at 0.4% of its peak at $s = 42$ cm. The full spread of frequencies is $5\sigma_{\nu_s}$; from TRANSVRS we find that this corresponds to a first cell radius of 5.9 mm and a last cell radius of 3.8 mm. Performing the sum Eq. (1.6) (and including the variation of $K_{s1}^{(m)}$ as obtained from TRANSVRS) we obtain the wakefield shown in Fig. 4. To better see the level of cancellation we plot the envelope of the wake $\hat{W}$ on a semi-log scale in Fig. 5. The dashed curve on this plot displays the Gaussian envelope of Eq. (1.5)[with σ_ν set to σ_{ν_s}] for comparison.

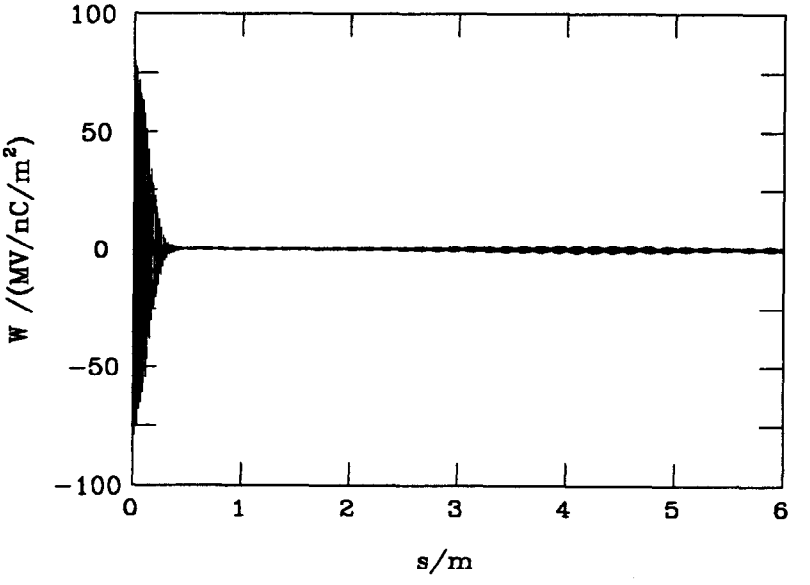

Fig. 4. The wakefield of the NLC structure assuming no coupling. The frequency distribution is Gaussian with $\sigma_{\nu_s}/\bar{\nu}_s = 2.5$ %.

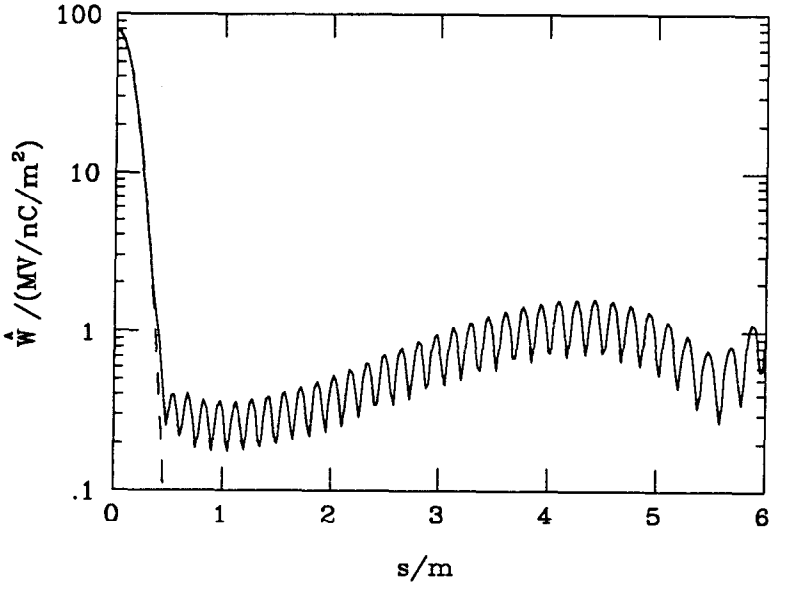

Fig. 5. The envelope of the wakefield shown in Fig. 4. The dashed curve displays the Gaussian envelope of Eq. (1.5) for comparison. Coupling between cells has been ignored here.

We see from the plots that the wakefield envelope begins at a peak value of 80 MV/nC/m^2. It does indeed drop as a Gaussian before the arrival of the second bunch, at $s = 42$ cm. At longer distances it no longer drops as a Gaussian; however it still remains quite small up to the position of the last (the 10^{th}) bunch at $s = 378$ cm. The saturation effect is due to the truncated tails in the Gaussian frequency distribution, and the relative amplitude at saturation is approximately given by $1/N$-$2/N$. Up to what value of s can we expect to believe the result? From Fig. 2 we see that the largest group velocity for geometry C (representing a cell near the beginning of the cavity) is $v_g/c \sim 0.1$. A conservative estimate then is that the uncoupled calculation is valid at least until $s \sim 3cL/v_g = 0.25$ m. In the next two chapters we will see that this estimate is too conservative, and that in fact the uncoupled results agree well with the more accurate calculations throughout our entire region of interest, *i.e.* the region up to $s = 4$ m.

From beam dynamics simulations[5] it appears that in order for the emittance growth due to the multibunch instability to be within acceptable limits we need the wakefield at the positions of bunches 2 through 10 to be on the order of 1% of the peak value, *i.e.* near 1 MV/nC/m^2, or less. Accordingly, we will consider as acceptable a wakefield with amplitude $\hat{W}(s) \leq 1$ MV/nC/m^2 over the range $s = 0.4$ m to $s = 3.8$ m. This criterion is more stringent than necessary (the wake only needs to be small at the actual positions of the trailing bunches). However, from the results of the uncoupled calculation it appears that this criterion can be met by the detuned version of the NLC structure. A major goal of this paper is to see how the cell-to-cell coupling affects this result.

2. Single Chain of Coupled Circuits

2.1 The Difference Equations

Let us begin by modelling our detuned structure by the single circuit chain shown in Fig. 6. We take loop m of the chain to represent cell m of the cavity. Let us assume the currents in the chain vary in time as $e^{2\pi i\nu t}$, with ν the resonant frequency of the chain and t the time. But instead of the currents $I_m(t)$ we will solve for the Fourier transform of the currents $i_m(\nu)$. The currents in loop m of the circuit chain satisfy the difference equation

$$\left(1-\frac{\nu_m^2}{\nu^2}\right) i_m + \frac{M_{m,m+1}}{2L_m} i_{m+1} + \frac{M_{m,m-1}}{2L_m} i_{m-1} = 0 \quad , \tag{2.1}$$

where the resonant frequency of the m^{th} circuit loop is given by

$$(2\pi\nu_m)^2 = \frac{1}{L_m C_m} \quad . \tag{2.2}$$

For N circuits Eq. (2.1) represents a system of N coupled equations. In order to symmetrize the problem let us change variable to

$$f_m \equiv i_m \nu_m \sqrt{L_m} = i_m/\sqrt{C_m} \quad . \tag{2.3}$$

Then Eq. (2.1) becomes

$$\left(\frac{1}{\nu_m^2}-\frac{1}{\nu^2}\right) f_m + \frac{\kappa_{m+\frac{1}{2}}}{2} f_{m+1} + \frac{\kappa_{m-\frac{1}{2}}}{2} f_{m-1} = 0 \quad , \tag{2.4}$$

where the equivalent coupling coefficient is

$$\kappa_{m\pm\frac{1}{2}} \equiv \frac{M_{m,m\pm1}}{\nu_m \nu_{m\pm1}\sqrt{L_m L_{m\pm1}}} = M_{m,m\pm1}\sqrt{C_m C_{m\pm1}} \quad . \tag{2.5}$$

We will allow $\kappa_{m\pm\frac{1}{2}}$ to be a positive or negative quantity depending on whether locally the cell-to-cell coupling is positive or negative. Sometimes, instead of $\kappa_{m\pm\frac{1}{2}}$ we may find it more convenient to use the relative coupling coefficient, defined by

$$\eta_{m\pm\frac{1}{2}} \equiv \kappa_{m\pm\frac{1}{2}} \nu_m \nu_{m\pm1} \quad , \tag{2.6}$$

when discussing coupling. (In Table 1 we give the resonator frequencies ν_m and relative coupling coefficients η appropriate for the representative cell geometries *A-G*.) Eq. (2.4) represents a linear, symmetric eigenvalue (ν^{-2}) eigenfunction (f_m) problem whose solutions can be obtained from readily available computer programs, once the variation of ν_m^{-2} and $\kappa_{m\pm\frac{1}{2}}$ is selected and once the boundary conditions at the end cells are specified.

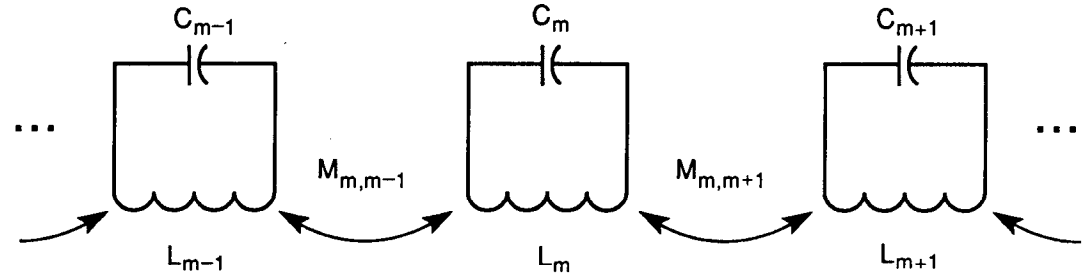

Fig. 6. A single chain circuit model of the accelerator structure.

In order to solve the problem we need to specify the boundary conditions. Typically the cavity has N full cells with the end cells connected to side tubes. For the first dipole band the frequencies are below the cut-off of these side tubes and power will not flow down them. For such a configuration, with the circuits indexed by $m = 1,2,\ldots,N$, we take as boundary conditions

$$f_0 = f_1 \ , \quad f_{N+1} = f_N \ , \quad \kappa_{\frac{1}{2}} = \kappa_1 \ , \quad \kappa_{N+\frac{1}{2}} = \kappa_N \quad , \tag{2.7}$$

with κ_1, κ_N, the coupling factors of cell 1 and cell N respectively. Another possible configuration are $N-2$ full cells ($m = 2, 3, \ldots, N-1$) with closed half cells at the ends ($m = 1, N$). In this case the appropriate boundary conditions might be

$$f_0 = f_2 \ , \quad f_{N+1} = f_{N-1} \ , \quad \kappa_{\frac{1}{2}} = \kappa_{\frac{3}{2}} \ , \quad \kappa_{N+\frac{1}{2}} = \kappa_{N-\frac{1}{2}} \quad . \tag{2.8}$$

There may be some question about our choice of boundary conditions. However, as we shall see later, the results for the NLC structure depend only weakly on the specific choice of boundary conditions.

If we substitute constant $\nu_m = \bar{\nu}$ and $\kappa_{m\pm\frac{1}{2}} = \kappa$ into Eq. (2.4) then we obtain the periodic solutions:

$$f_m = f \cos m\phi \quad , \tag{2.9}$$

and

$$\frac{1}{\nu^2} = \frac{1}{\bar{\nu}^2} + \kappa \cos\phi \quad . \tag{2.10}$$

Clearly the variation of ν^{-2} is linear with $\cos\phi$ for this single circuit chain. When κ is positive the wave is a forward wave, when it is negative it is a backward wave. Note that $\bar{\nu}$ gives the frequency of the $\pi/2$ mode. The boundary conditions for a cavity with N full cells [Eqs. (2.7)] restrict the phase advance to the values

$$\phi_p = \frac{(p-1)\pi}{N} \quad , \quad p = 1, 2, \ldots, N \quad . \tag{2.11}$$

Note that for these boundary conditions the pi mode is not a solution. With the boundary conditions given by Eq. (2.8) the solutions are the same but with the phase advance restricted to

$$\phi_p = \frac{(p-1)\pi}{(N-1)} \quad , \quad p = 1, 2 \ldots N \quad . \tag{2.12}$$

2.2 Differential Equation for a Single Circuit Chain

Let us return to Eq. (2.4), the difference equation for the eigenfunctions of our coupled circuit model. Let us change variable from f_m to

$$F_m \equiv (-1)^m f_m \tag{2.13}$$

since the modes travelling with phase velocity near c are near the pi mode of the structure (see Fig. 2). We can therefore treat F_m as a slowly varying function of m. In this case we write Eq. (2.4) as

$$\left(\frac{1}{\nu_m^2} - \frac{1}{\nu^2} - \frac{\kappa_{m+\frac{1}{2}} + \kappa_{m-\frac{1}{2}}}{2}\right) F_m - \left(\frac{\kappa_{m+\frac{1}{2}} + \kappa_{m-\frac{1}{2}}}{4}\right)(F_{m+1} + F_{m-1} - 2F_m) - \left(\frac{\kappa_{m+\frac{1}{2}} - \kappa_{m-\frac{1}{2}}}{2}\right)\left(\frac{F_{m+1} - F_{m-1}}{2}\right) = 0 \quad . \tag{2.14}$$

Introducing the continuous variables

$$x(m) = \frac{1}{\nu_m^2} - \frac{\kappa_{m+\frac{1}{2}} + \kappa_{m-\frac{1}{2}}}{2} \quad , \tag{2.15}$$

$$\kappa(m) = \frac{\kappa_{m+\frac{1}{2}} + \eta_{m-\frac{1}{2}}}{2} \quad , \quad \kappa'(m) = \kappa_{m+\frac{1}{2}} - \kappa_{m-\frac{1}{2}} \quad , \tag{2.16}$$

we proceed to the limit of small rate of change and obtain the differential equation

$$\frac{\kappa(m)}{2}\frac{d^2F}{dm^2} + \frac{\kappa'(m)}{2}\frac{dF}{dm} + [\lambda - x\,(m)]\,F = 0 \quad . \tag{2.17}$$

The parameter $\lambda \equiv \nu^{-2}$.

Let us now assume a linear variation of $x(m)$ and $\kappa(m)$ in the form

$$x(m) = \lambda_0 + \gamma\,(m - m_0) \quad , \quad \kappa(m) = \alpha\,(m - m_0) \quad , \tag{2.18}$$

where m_0 is the cell number where the coupling constant vanishes and λ_0 gives the frequency of this cell. (We see from Table 1 that, over the geometry range repre-

sented by cells A-E, this linear approximation is valid.) Substituting Eqs. (2.18) into Eq. (2.17) we obtain

$$\frac{d^2F}{dm^2} + \frac{1}{m-m_0}\frac{dF}{dm} - \frac{2}{\alpha}\left[\gamma - \frac{(\lambda-\lambda_0)}{(m-m_0)}\right]F = 0 \quad . \tag{2.19}$$

We now change independent variable from cell number m to

$$u = \sqrt{\frac{2\gamma}{\alpha}}\,(m-m_0) \tag{2.20}$$

and find

$$\frac{d^2F}{du^2} + \frac{1}{u}\frac{dF}{du} + \left(\frac{\sigma}{u} - 1\right)F = 0 \quad , \tag{2.21}$$

where the eigenvalue λ is now redefined as

$$\sigma = (\lambda - \lambda_0)\sqrt{\frac{2}{\alpha\gamma}} \quad . \tag{2.22}$$

Equation (2.21) corresponds to the Schrödinger equation for a hydrogen atom, except for the absence of a factor 2 in the $F'(u)$ term. Its solutions are therefore related to the Laguerre polynomials for angular momentum one half. But the analysis of Eq. (2.21) is sufficiently simple so that we can directly obtain the series solutions in the form

$$F(u,\sigma) = e^{-u}\sum_{n=0}^{\infty}\frac{(-1)^n(2u)^n}{(n!)^2}\frac{\Gamma(\frac{\sigma+1}{2})}{\Gamma(\frac{\sigma+1}{2}-n)} \quad . \tag{2.23}$$

If the series in Eq. (2.23) does not truncate, the behavior of $F(u,\sigma)$ for $u > \sigma$ will diverge exponentially, making it impossible for $F(u,\sigma)$ to satisfy the boundary

condition at the end of the cavity. Thus the modes are discrete with the index p, and are

$$F_p(u) = e^{-u} \sum_{n=0}^{p} \frac{(-1)^n (2u)^n p!}{(n!)^2 (p-n)!} \quad , \tag{2.24}$$

where

$$\sigma = 2p + 1 \ , \ p = 0, 1, 2, \ldots \quad . \tag{2.25}$$

The solution in Eq. (2.24) applies for $u > 0$ and has a significant value only until the (approximate) turning point at $u = \sigma = 2p + 1$, beyond which $F_p(u)$ decreases exponentially, as can be seen from Eq. (2.21). Thus the mode represented in Eq. (2.24) is localized to the region between $u = 0$ and $u = 2p + 1$. Similarly, for $\sigma < 0$, the modes are localized between $u = 0$ and $u = -(2p + 1)$ and the same functions as in Eq. (2.24) are obtained with $u \rightarrow -u$ and

$$\sigma = -(2p + 1) \ , \ p = 0, 1, 2, \ldots \quad . \tag{2.26}$$

Since λ varies linearly, the modes are equally spaced in frequency, a consequence of our assumption that $x(m)$ and $\kappa(m)$ are linear functions of m. We see that the ratio of the spacing of the normal mode frequencies $\delta\nu$ to the spacing of the cell frequencies $\delta\nu_m$ is given by

$$\frac{\delta\nu}{\delta\nu_m} = -\frac{\sqrt{2\alpha\gamma}}{\alpha + \gamma} \quad . \tag{2.27}$$

The preceding analysis is limited in at least two respects. First, the actual modes are discrete functions of the variable m and the continuous function in Eq. (2.24) is only an approximation, particularly if $(2\gamma/\alpha)^{1/2}$ in Eq. (2.20) is not small. Second, the location at which $F(u)$ becomes exponential, $u > \sigma$ or $-u < -\sigma$, must lie well within the cavity. If this is not the case, the modes are oscillatory near one of the walls and the eigenvalues, which depart from Eqs. (2.25) and (2.26), are not easily obtained analytically.

We can also construct an approximate result for the more general case, using a WKB like solution of Eq. (2.17) neglecting the first derivative term. In this case, we have

$$\frac{d^2F}{dm^2} + 2\frac{(\lambda - x(m))}{\kappa(m)}F \cong 0 \quad , \tag{2.28}$$

with F being oscillatory between m_0, where κ vanishes, and m_1, where $x(m_1) = \lambda$. The eigenvalue condition is therefore

$$\int_{m_0}^{m_1} dm \left(\frac{2[\lambda - x(m)]}{\kappa(m)}\right)^{1/2} \cong p\pi \quad . \tag{2.29}$$

With linear variation of $x(m)$ and $\kappa(m)$, we have

$$\sqrt{\frac{2\gamma}{\alpha}} \int_{m_0}^{m_1} dm \sqrt{\frac{m_1 - m}{m - m_0}} = \sqrt{\frac{\gamma}{2\alpha}}\,\pi\,(m_1 - m_0) = p\pi \tag{2.30}$$

where

$$m_1 - m_0 = \frac{\lambda - \lambda_0}{\gamma} \quad . \tag{2.31}$$

Thus

$$p = \frac{\lambda - \lambda_0}{\sqrt{2\alpha\gamma}} = \frac{\sigma}{2} \quad , \tag{2.32}$$

in agreement with Eq. (2.25) except for the 1 which most likely comes from the phase shifts at $m = m_0$ and m_1, and from the neglect of the first derivative term. An advantage of using Eq. (2.29) for the eigenvalues is that it can lead to approximate results for various non-linear forms for $x(m)$ and $\kappa(m)$.

The calculation of the kick factor for the general case will be described in detail in the next section. For easier comparison with the numerical results to be presented later let us here define a normalized kick factor K'_p as

$$K'_p = \frac{\left|\sum_{m_0}^{m_1} F_m e^{im\psi}\right|^2}{\sum_{m_0}^{m_1} F_m^2} \cong \frac{\left|\int_0^\infty du F_p(u) e^{iu\bar{\psi}}\right|^2}{\int_0^\infty du F_p^2(u)} \tag{2.33}$$

where $\psi = (2\gamma/\alpha)^{1/2}\bar{\psi}$ is the difference of the phase shift per cell from π. Remarkably, the integrals in the numerator and denominator in Eq. (2.33) can be evaluated exactly for the modes in Eq. (2.24) and are independent of p. In fact, we find

$$K'_p = \frac{2}{1+\bar{\psi}^2} \quad . \tag{2.34}$$

Finally, we point out that in terms of the normalized kick factor the normal kick factor (to be presented in the next section) is given by $K_p \approx K'_p \bar{K}_{sp}$, with $\bar{K}_{sp}$ equal to the kick factor for the geometry of the cell on which the mode is centered.

2.3 The Kick Factors

Equation (2.4) together with the appropriate boundary conditions can be used with tapered parameters ν_m and $\kappa_{m\pm\frac{1}{2}}$ to find the eigenmodes of a detuned structure. In order to find the kick factors of the cavity we first need to make some more correspondences between the circuit model and the cavity. Let us take the voltage drop across the capacitor in loop m of the circuit to represent the longitudinal voltage the beam loses (to the dipole modes) in cell m of the cavity. Let us further take the value of this capacitor to be $C_m = (2\mathcal{K}_s^{(m)} x_e x L)^{-1}$, with $\mathcal{K}_s^{(m)} = 2\pi\nu_s^{(m)} K_s^{(m)}/c$ the loss factor of the dipole mode for the periodic structure with the dimension of cell m (which is obtained using TRANSVRS); x_e is the driving charge offset, x is the test charge offset, and L is the cell length. Now let us assume the cavity is empty at time $t = 0$. Let us assume also that the driving charge enters the cavity at time $t = \frac{1}{2}L/c$ and reaches the center of cell m at $t = mL/c$. To represent this in the circuit model we take as our $2N$ initial conditions (assuming we have N loops) that at time $t = 0$ both the current and the voltage in every loop are zero. In addition, in each loop m we include as driving term the current source $-q_e\delta(t - mL/c)$ in parallel with the capacitor. Then, since we already know the Fourier transform of the eigenfunctions of the system, we represent the Fourier transform of the solution of the new, driven equations by a sum over these eigenfunctions (for a discussion of this method see, for example, Ref. 16). Performing

the inverse Fourier transform we obtain the time evolution of the currents in the circuit. Then finally, it is a simple matter to obtain the kick factors.

Before beginning, let us briefly discuss one conceptual problem with using our circuit to model the time development of the fields in a multi-cell cavity.[⋆] In a real cavity causality holds and an excitation in cell 1 cannot arrive in cell m until the time $(m-1)L/c$ later. For our circuit model, however, there is no time delay: some current reaches every loop of the circuit immediately after the excitation in loop 1. However, this is not a serious problem if the relative cell-to-cell coupling η is small (as is the case for the NLC structure). In such a case the initial growth of the current in loop m is a factor $(M_{m,m+1}/L_m)^{m-1} = \eta^{m-1}$ smaller than the initial growth in loop 1. For our problem of sequentially excited loops this implies that any precursor voltage—*i.e.* voltage getting ahead of the excitation front—will be small.

Taking the Fourier transform of the driving terms discussed above has the effect of adding

$$h_m = \frac{q_e}{\nu^2\sqrt{C_m}} e^{-2\pi i m \nu L/c} \tag{2.35}$$

to the right hand side of our matrix equation, Eq. (2.4). In vector notation the eigenvalue equation that we solved, Eq. (2.4), is written as

$$M\mathbf{f}^{(p)} = \lambda_p \mathbf{f}^{(p)} \quad , \tag{2.36}$$

with M the matrix of the system, $\mathbf{f}^{(p)}$ the p^{th} eigenfunction, and $\lambda_p = \nu_p^{-2}$ the p^{th} eigenvalue. In this notation the m^{th} element of a vector gives the value of the parameter in cell m. We want to solve

$$M\mathbf{g} - \lambda\mathbf{g} = \mathbf{h} \quad , \tag{2.37}$$

⋆ This problem was pointed out by Matt Sands.

with $\lambda = \nu^{-2}$, for the vector $\mathbf{g}$. To do this we expand $\mathbf{g}$ and $\mathbf{h}$ in terms of the eigenfunctions. Then Eq. (2.37) leads to

$$\mathbf{g} = \sum_p \frac{\mathbf{f}^{(p)}}{\lambda_p - \lambda} \left[\frac{\mathbf{f}^{(p)} \cdot \mathbf{h}}{|f^{(p)}|^2} \right] \quad , \tag{2.38}$$

with $\mathbf{a} \cdot \mathbf{b}$ representing the dot product of vectors $\mathbf{a}$ and $\mathbf{b}$ and $|a|^2 \equiv \mathbf{a} \cdot \mathbf{a}$. In obtaining Eq. (2.38) we have used the orthogonality of the eigenfunctions, which holds because our matrix is real and symmetric. In addition we have assumed the system is non-degenerate.

Going back to the time domain we find that in loop m of the circuit

$$\begin{aligned} G_m(t) &= \int_{-\infty}^{\infty} d\nu \, g_m(\nu) e^{2\pi i \nu t} \\ &= q_e \sum_p \frac{f_m^{(p)} \nu_p^2}{|f^{(p)}|^2} \sum_n \frac{f_n^{(p)}}{\sqrt{C_n}} \int_{-\infty}^{\infty} \frac{d\nu}{\nu^2 - \nu_p^2} e^{2\pi i \nu (t - nL/c)} \quad . \end{aligned} \tag{2.39}$$

The integral in the above equation contains two poles, at $\nu = \pm \nu_p$. We add a small positive imaginary part to these pole positions. If $(t - nL/c) > 0$ we close the integration loop in the upper half plane, else in the lower half plane. The result is

$$G_m(t) = -2\pi q_e \sum_p \frac{f_m^{(p)} \nu_p}{|f^{(p)}|^2} \sum_n \Theta(t - nL/c) \frac{f_n^{(p)}}{\sqrt{C_n}} \sin 2\pi \nu_p (t - nL/c) \quad , \tag{2.40}$$

with $\Theta(t) = 0$ for $t < 0$, $\Theta(t) = 1$ for $t > 0$. From our definition of f_m [see Eq. (2.4)] we see that the current in the inductor in loop m is given by $I_m = \sqrt{C_m} G_m(t)$. To get the current in the capacitor we need to add the driving current to this. The voltage drop across the capacitor is given by

$$\begin{aligned} V_{zm}(t) &= \frac{1}{C_m} \int_0^t I_m(t') \, dt' \; + \; \frac{q_e}{C_m} \Theta(t - mL/c) \\ &= \frac{q_e}{\sqrt{C_m}} \sum_p \frac{f_m^{(p)}}{|f^{(p)}|^2} \sum_n \Theta(t - nL/c) \frac{f_n^{(p)}}{\sqrt{C_n}} \cos 2\pi \nu_p (t - nL/c) \; . \end{aligned} \tag{2.41}$$

The voltage drop across the capacitor represents the energy loss of a test particle to the dipole modes of the cavity. But in this paper we are concerned primarily with the transverse kick that the test particle experiences from the dipole mode. By using the Panofsky-Wenzel theorem[17] we can obtain the transverse kick from the longitudinal one, *i.e.* the transverse kick $V_m(t) = (c/x)\int^t dt'\, V_{zm}(t')$. Thus we find that the transverse kick in cell m is given by

$$V_m(t) = 2q_e x_e L \sum_p \frac{f_m^{(p)}\sqrt{K_s^{(m)}\nu_s^{(m)}}}{\nu_p |f^{(p)}|^2} \sum_n \Theta(t-nL/c) f_n^{(p)} \sqrt{K_s^{(n)}\nu_s^{(n)}} \sin 2\pi\nu_p(t-nL/c)\,. \tag{2.42}$$

Eq. (2.42) implies that the amplitudes and phases of the modes after the driving particle has left the cavity are given by

$$V_m(t) = \sum_p V_m^{(p)} \sin(2\pi\nu_p t - \theta_p) \qquad t > NL/c\,, \tag{2.43}$$

with

$$V_m^{(p)} = \frac{2q_e x_e L f_m^{(p)}\sqrt{K_s^{(m)}\nu_s^{(m)}}}{\nu_p |f^{(p)}|^2} \left| \sum_n f_n^{(p)} \sqrt{K_s^{(n)}\nu_s^{(n)}}\, e^{in\varphi_p} \right| \quad , \tag{2.44}$$

$$\tan\theta_p = \frac{\sum_n f_n^{(p)}\sqrt{K_s^{(n)}\nu_s^{(n)}}\,\sin(n\varphi_p)}{\sum_n f_n^{(p)}\sqrt{K_s^{(n)}\nu_s^{(n)}}\,\cos(n\varphi_p)} \quad , \tag{2.45}$$

and $\varphi_p = 2\pi\nu_p L/c$.

Let us return to the voltage equation that is valid for all time, Eq. (2.42). This equation can also be used to obtain the total voltage a test particle, following a distance s behind the driving charge, experiences in cell m of the cavity, $\tilde{V}_m(s)$. This quantity is given by

$$\tilde{V}_m(s) = V_m\left(\frac{mL+s}{c}\right) \quad . \tag{2.46}$$

Summing up the contributions of all the cavity cells we obtain the total kick felt by the test charge

$$\tilde{V}(s) = \sum_m \tilde{V}_m(s) \quad . \tag{2.47}$$

This equation can be combined with Eq. (2.42), (2.46), to give the general form of the induced voltage.

Now, let us assume that the couplings η are small so that we can ignore the effects of any precursor voltages, and that therefore we can approximate $\tilde{V}(s) = 0$ for $s < 0$. This relation combined with Eqs. (2.42), (2.46), (2.47), leads to

$$\tilde{V}(s) \approx 2q_e x_e NL \sum_p K_p \sin \frac{2\pi\nu_p s}{c} \qquad s > 0, \tag{2.48}$$

with the kick factor for mode p given by

$$K_p = \frac{|\sum_n f_n^{(p)} \sqrt{K_s^{(n)} \nu_s^{(n)}} e^{in\varphi_p}|^2}{N\nu_p |f^{(p)}|^2} \quad . \tag{2.49}$$

Eq. (2.48), which represents the induced voltage of the cavity, is of the form that we expect. With weak cell-to-cell coupling the results of this equation should agree well with the more exact calculation of the induced voltage, and in the simulations of the NLC cavity, to be presented in Sec. 2.5, we will see that this is indeed the case. In a similar vein, when the coupling is weak we also expect the kick profile $\tilde{V}_m(s)$ to be given by a simplified equation valid for all $s > 0$:

$$\tilde{V}_m(s) \approx \sum_p V_m^{(p)} \sin \left[\frac{2\pi\nu_p}{c}(mL + s) - \theta_p \right] \qquad s > 0. \tag{2.50}$$

Eqs. (2.49) gives us the kick factors of the cavity modes. How do the parameters in the equation correspond, in terms of the properties of the circuit model, to what we expect in a cavity? Recall that for any dipole mode of a cavity p the loss

factor $\mathcal{K}_p = 2\pi\nu_p K_p/c$ is given by the ratio of the square of the maximum voltage gained by a test particle (with respect to time of entry into the cavity) to the product $4x_e xNL$ times the energy stored in the mode.[15] From the meaning of the parameters of Eq. (2.49) in terms of the circuit parameters we see that Eq. (2.49) gives approximately, though not exactly, the proper ratio of the maximum voltage squared and the energy stored in the modes of the circuit chain.

2.4 Losses

If we run the computer program URMEL[18] we find that for a periodic, copper cavity with cell geometry anywhere in the range A-E the Q factor, near pi phase advance, is nearly constant and given by 6500 (TRANSVRS does not compute the Q's). This size of Q implies that the wakefield does not damp to $1/e$ until 40 m behind the driving bunch. So the wall losses are not very important for the specific goal of this paper, that of having small wakefields between 0.4 m and 3.8 m behind the driving bunch. However, for completeness, we will describe briefly how we can include losses in our circuit model. Once we have the Q's of the normal modes, in addition to the frequencies and the kick factors, then we have the complete long range picture of the wakefields.

To add damping to our circuit model we add to each circuit loop m a resistor R_m in series with the capacitor. The effect on our homogeneous difference equation, Eq. (2.4), is the addition of the term $-if_m/(Q_m\nu_m\nu)$ on the left hand side, with the quality factor $Q_m = 2\pi\nu_m L_m/R_m$. Now our eigenvalue problem has become complex, non-hermitian, and non-linear. In theory we can solve this problem by stepping in frequency to find the zeros of the determinant of the matrix; these positions give the eigenvalues, and then we can back substitute to find the eigenfunctions (as is done, for example, in the program TRANSVRS). However, here we will develop the loss calculation using a perturbation approach. This approach should be sufficient for detuned structures with smoothly varying parameters so long $1/Q_m$ is always small compared to 1. (If for any m, $1/Q_m$ is *not* small we would doubt that there would be *any* validity to our equivalent circuit model.)

Our perturbation technique (see, for example, Ref. 16) is also applied to finding the losses of a multi-cell cavity by J. Rees in Ref. 9.

Let us begin by writing our original eigenvalue problem in vector notation:

$$M\mathbf{f}^{(p)} = \lambda_p \mathbf{f}^{(p)} \quad . \tag{2.51}$$

Our perturbed eigenvalue equation is

$$(M + M')\mathbf{g}^{(p)} = (\lambda_p + \lambda'_p)\mathbf{g}^{(p)} = \tilde{\lambda}_p \mathbf{g}^{(p)} \quad , \tag{2.52}$$

with $M + M'$ the new matrix, and (for mode index p) $\mathbf{g}^{(p)}$ the new eigenfunction, and $\lambda_p + \lambda'_p = \tilde{\lambda}_p$ the new eigenvalue. The new eigenfrequencies, which in our case are complex, are given by $\tilde{\nu}_p^2 = 1/\tilde{\lambda}_p$. We expand the new eigenfunctions in terms of the original eigenfunctions as

$$\mathbf{g}^{(p)} = \mathbf{f}^{(p)} + \sum_{q \neq p} c_{qp} \mathbf{f}^{(q)} \quad . \tag{2.53}$$

Substituting Eq. (2.53) into Eq. (2.52), and using Eq. (2.51), we obtain

$$\sum_{q \neq p} c_{qp} \lambda_q \mathbf{f}^{(q)} + M' \mathbf{f}^{(p)} = \lambda_p \sum_{q \neq p} c_{qp} \mathbf{f}^{(q)} + \lambda'_p \mathbf{f}^{(p)} \tag{2.54}$$

In Eq. (2.54) we have assumed the perturbations are small, and have kept only first order terms. Taking the dot product of $\mathbf{f}^{(p)}$ with Eq. (2.54) we obtain the perturbation to the eigenvalues:

$$\lambda'_p = \frac{\mathbf{f}^{(p)} \cdot M' \mathbf{f}^{(p)}}{|f^{(p)}|^2} \quad . \tag{2.55}$$

Taking the dot product of $\mathbf{f}^{(q')}$ with Eq. (2.54) we obtain the coefficients that give us the perturbation to the eigenfunctions:

$$c_{qp} = \frac{\mathbf{f}^{(q)} \cdot M' \mathbf{f}^{(p)}}{(\lambda_p - \lambda_q)|f^{(q)}|^2} \quad . \tag{2.56}$$

It is not easy to quantify when this perturbation technique is valid. Normally, the criterion for the perturbation to be considered small, and this technique to be valid, is that for all $q \neq p$ the ratio $c_{qp}/|f^{(p)}|$ be small compared to 1.

For our equivalent circuit M' is a diagonal matrix; in Eqs. (2.55), (2.56), its elements are given by

$$M'_{mm} = -\frac{i}{Q_m \nu_m \tilde{\nu}_p} \quad . \tag{2.57}$$

Note that if for all m, $Q_m = Q$ and $\nu_m = \bar{\nu}$ we need not perform the perturbation calculation. In this case the solution matrix is the same as for the unperturbed case, and the perturbed eigenfunctions are the same as the unperturbed ones. Only the eigenvalues change; they are given by

$$\tilde{\lambda} = \frac{1}{\tilde{\nu}_p^2} = \frac{1}{\nu_p^2} - \frac{i}{Q\bar{\nu}\tilde{\nu}_p} \quad . \tag{2.58}$$

The real and imaginary parts of the eigenfrequencies are then

$$\Re\mathrm{e}(\tilde{\nu}_p) = \nu_p \sqrt{1 - \left(\frac{\nu_p}{2Q\bar{\nu}}\right)^2} \quad , \quad \Im\mathrm{m}(\tilde{\nu}_p) = \frac{\nu_p^2}{2Q\bar{\nu}} \quad . \tag{2.59}$$

For $1/Q$ small the real part of the eigenfrequency is the same as the unperturbed eigenfrequency. And under this assumption the second relation of Eq. (2.59) implies that the mode quality factors are given by $Q_p = Q\bar{\nu}/\nu_p$.

For our detuned cavity we take $Q_m = Q$ to be constant and allow ν_m to vary slightly. Then Eq. (2.56) suggests that the largest value of $c_{qp}/|f^{(p)}|$ is $\sim 1/Q$.

2.5 Simulation Results

A computer program was written to solve the coupled difference equations Eq. (2.4) with the boundary conditions Eqs. (2.7). In order to easily obtain the constants in the equations, *i.e.* ν_m and $\kappa_{m\pm\frac{1}{2}}$ (or equivalently $\eta_{m\pm\frac{1}{2}}$), for any combination of cell geometries a table was first generated using the computer program

TRANSVRS. For the 7 representative cavity geometries *A-G* (see Table 1) the synchronous frequency ν_s, the kick factor K_s, the zero mode frequency ν_0 and the pi mode frequency ν_π were obtained. The resonator frequencies and the relative coupling factors for these cavities are then taken to be

$$\nu_m = \sqrt{\frac{2\nu_\pi^2\nu_0^2}{\nu_\pi^2+\nu_0^2}} \qquad \text{and} \qquad \eta = \frac{\nu_\pi^2-\nu_0^2}{\nu_\pi^2+\nu_0^2} \quad . \tag{2.60}$$

Once this table has been generated then for any intermediate values of ν_s (we often find it convenient to designate cell geometry by ν_s) we obtain a, K_s, ν_m, and η by means of cubic spline interpolation. The parameter $\kappa_{m\pm\frac{1}{2}} = \frac{1}{2}(\eta_m + \eta_{m\pm1})/(\nu_m\nu_{m\pm1})$. In Fig. 7 we display the coupled frequencies obtained by our program for cavities with 6 identical cells, for the cavity geometries *A-G* (the plotting symbols), and compare them to the TRANSVRS results (the curves). Although, as discussed previously, the single circuit solutions do not agree well with the dispersion curves over the whole range of phase advance, due to our definition of ν_m and η [see Eq. (2.60)] they do agree well near the ends of the curves. In particular, in the important vicinity of the synchronous point the agreement is quite good.

As our first tapered example, in order to verify some of the results of Section 2.2, we consider a 200 cell, NLC type structure but with a linear variation of ν_s as we move from the beginning to the end of the structure. We take the full-width of the frequency distribution to be $\Delta\nu_s/\bar{\nu}_s = 9$ % and $\bar{\nu}_s = 15.25$ GHz. In Fig. 8 we display the resulting coupled mode frequencies ν (given in order of increasing frequency) and the normalized kick factors K' for this example. The dashes in Fig. 8a connect the uncoupled solutions. We see from Fig. 8 that for most of the modes—for modes $\sim$ 60 to 170—the frequency distribution is uniform and the normalized kick factors are approximately constant; outside this range of modes the kick factors rapidly drop to zero. We also see that the separation of frequencies is larger than that assumed by the uncoupled calculation; over the linear range we find that $\delta\nu/\delta\nu_s = 1.65$. Also, the total frequency spread is much larger; for the

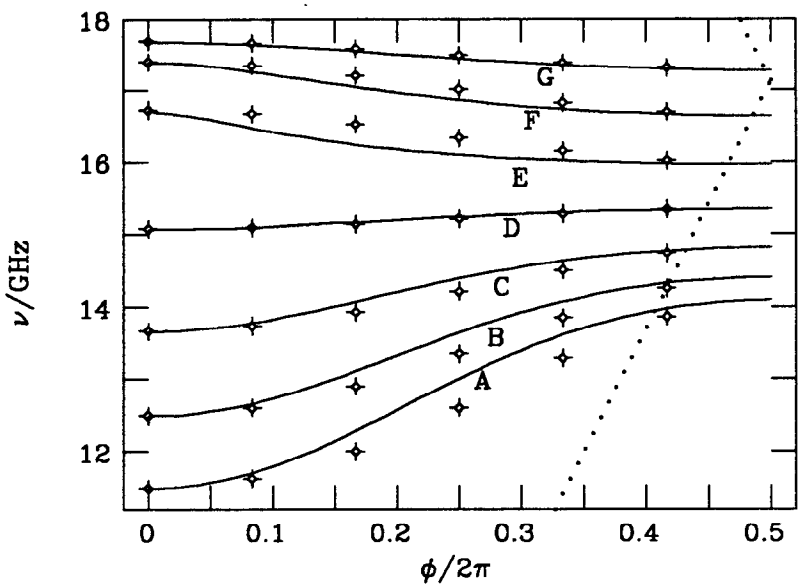

Fig. 7. The single circuit chain solutions with 6 identical cells (the plotting symbols). For comparison the dispersion curves obtained from TRANSVRS are also shown. The dots give the speed of light line.

coupled calculation the lowest frequency 13.2 GHz equals the lowest frequency of the dispersion curve that corresponds to the first cell geometry (roughly half-way between cell B and cell C of Table 1) while the highest frequency 16.6 GHz equals the highest frequency of the dispersion curve that corresponds to the last cell geometry (near cell E). However, the range of important frequencies—those frequencies for which the kick factor is significant—is approximately the same as the range of synchronous frequencies, 14.5 GHz to 16 GHz.

A uniform mode distribution and constant kick factors were both predicted in Section 2.2, where we replaced the difference equations by a differential equation. We find this agreement with the form of the results (for modes 60-170) in spite of the fact that $\sqrt{2\gamma/\alpha}$, the parameter which needs to be small for the analytical approximation to be valid, is 1.4, and is not small. In more detail we see that the value of $\delta\nu/\delta\nu_m$ obtained from the simulation is 0.9, which is only in rough agreement with the analytical value of 0.7 obtained from Eq. (2.27). In addition, we see that the value of the kick factors in the linear regime, 1.65, agrees well

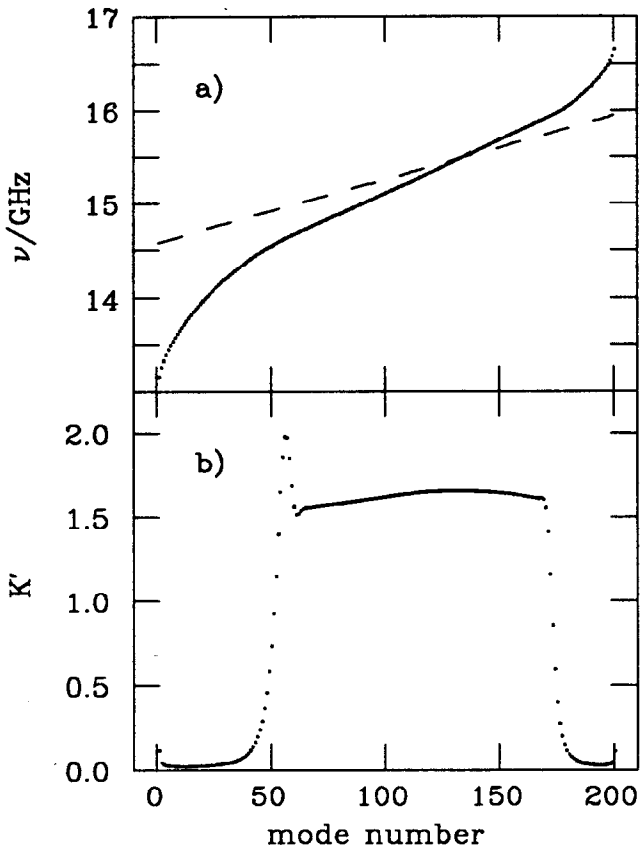

Fig. 8. The coupled mode frequencies ν (a) and the normalized kick factor K' (b) of a 200 cell structure with linear frequency variation and with full spread $\Delta\nu_s/\bar{\nu}_s = 9\ \%$. The dashes [in (a)] connect the uncoupled solutions.

with the analytical result, 1.80 (we have taken as typical value of $\bar{\psi}$ 0.35). In Fig. 9 we display the mode patterns [the values of $f_m^{(p)}\sqrt{K_s^{(m)}\nu_s^{(m)}}$] for every 10^{th} mode scaled arbitrarily. Each frame is a bar graph, with abscissa giving the cell number, ranging from cell $m = 0$ to 200. The plots, for modes 60-170, confirm the expectation implied in Eq. (2.29) that the modes are localized, and that the limits of their extent are approximately given by the cell for which the cell frequency equals the mode frequency and the cell for which the coupling goes to zero. (Note that the localization of the modes in the NLC structure was also found in Ref. 11.) In addition, we clearly see that the modes that depart from the uniform frequency

distribution and the constant kick factor (modes 1-60 and 170-200) are exactly those modes which reach the end walls of the structure.

Fig. 10 is our standard plot applied to this example. In the standard plot panel (a) shows the mode spectrum and panel (b) the kick factor *vs* frequency, including now the variation of the kick factor for a single cell with cell geometry. Panel (c) gives the product of the loss factor times the mode density, which in the smooth approximation is the Fourier transform of the wakefield [see Eq. (1.2)]. And panel (d) shows the wakefield envelope. In panels (a)-(c) 200 dots give the solutions of the eigenvalue problem, and the dashed curve represents, for comparison, the uncoupled results. In Fig. 10a we clearly see that the range over which the frequency distribution is linear is the same as the synchronous frequency range. In panel (b) we note that the (unnormalized) kick factor has a tilted top, reflecting the fact that the higher frequency cells, those more toward the end of the structure, interact more strongly with the beam. In panel (c) we see that the coupled result for $K\Delta n/\Delta\nu$ is very similar to the uncoupled result; one difference is that this function now has small tails. And in panel (d) we note the $\sin \beta s/\beta s$ behavior of the wakefield, which is due to the sharp edges of $K\Delta n/\Delta\nu$. The wakefield drops too slowly and is unacceptable for NLC needs. At the spacing of the second bunch, at $s = 42$ cm, the wakefield amplitude is 18 MV/nC/m^2; the requirement is that it be $\lesssim 1$ MV/nC/m^2.

The situation is clearly improved if we use a Gaussian distribution of cell parameters. In particular we choose an rms width $\sigma_{\nu_s}/\bar{\nu}_s = 2.5$ % (keeping the central frequency at $\bar{\nu} = 15.25$ GHz). This is the same structure for which, in Section 1.3, we presented a wakefield for the uncoupled calculation (see Fig. 5). The coupled results are shown in Fig. 11. In panel (d), as an aid to the eye, we again display the smooth approximation, Eq. (1.5) with σ_ν set to σ_{ν_s}, by the dashed curve. In Fig. 11a we see that the peak of the frequency distribution is 1.7 times that for the uncoupled calculation. In frame (b) we note that for a structure detuned according to a Gaussian distribution the kick factors vary as a smooth function of frequency, and they again become small outside the synchronous

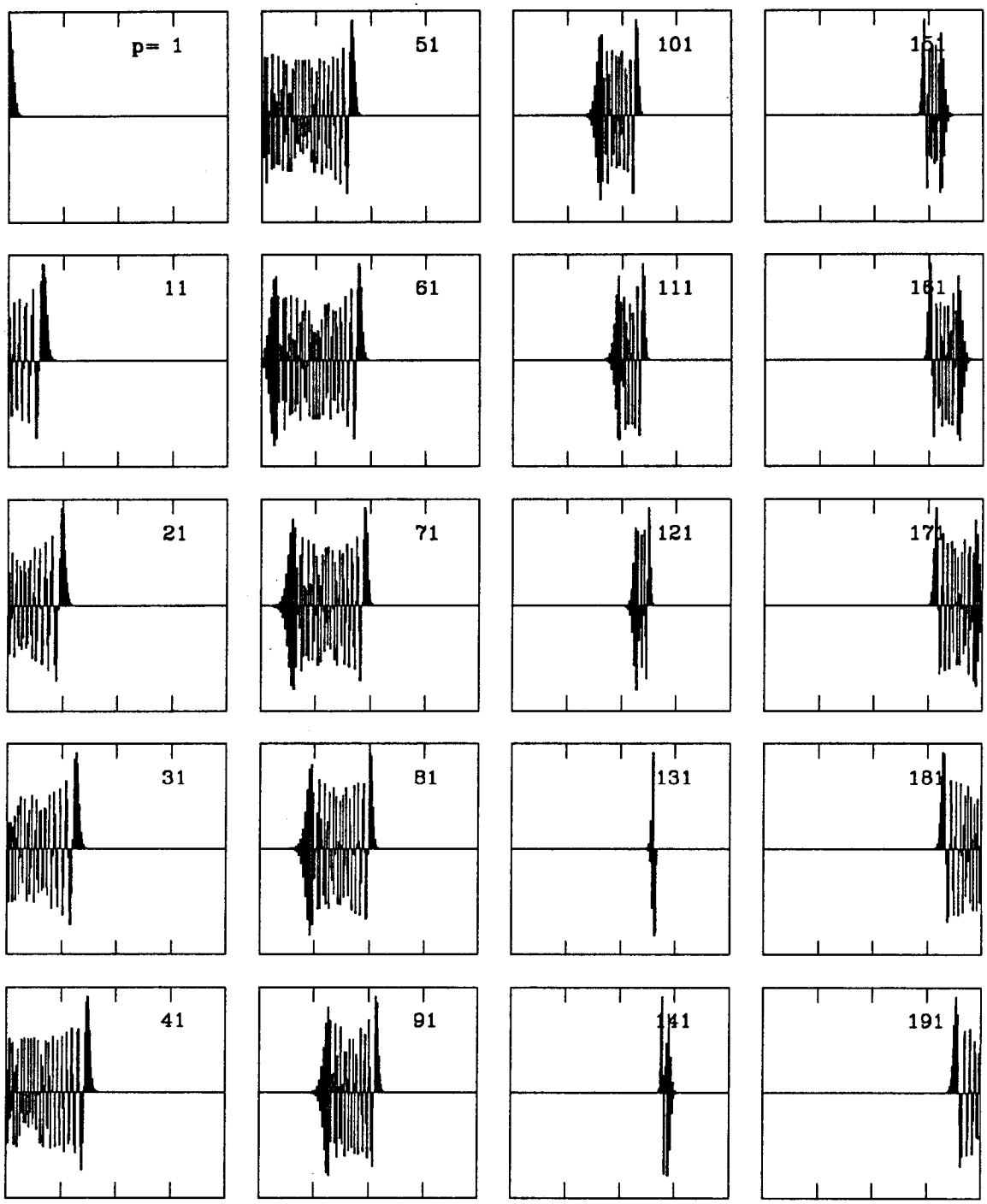

Fig. 9. Some mode patterns. The plots give $f_m^{(p)}\sqrt{K_s^{(m)}\nu_s^{(m)}}$ scaled arbitrarily. The abscissas give the cell number, ranging from $m = 0$ to $m = 200$. The distribution in ν_s is uniform with full-width $\Delta\nu_s/\bar{\nu}_s = 9$ %.

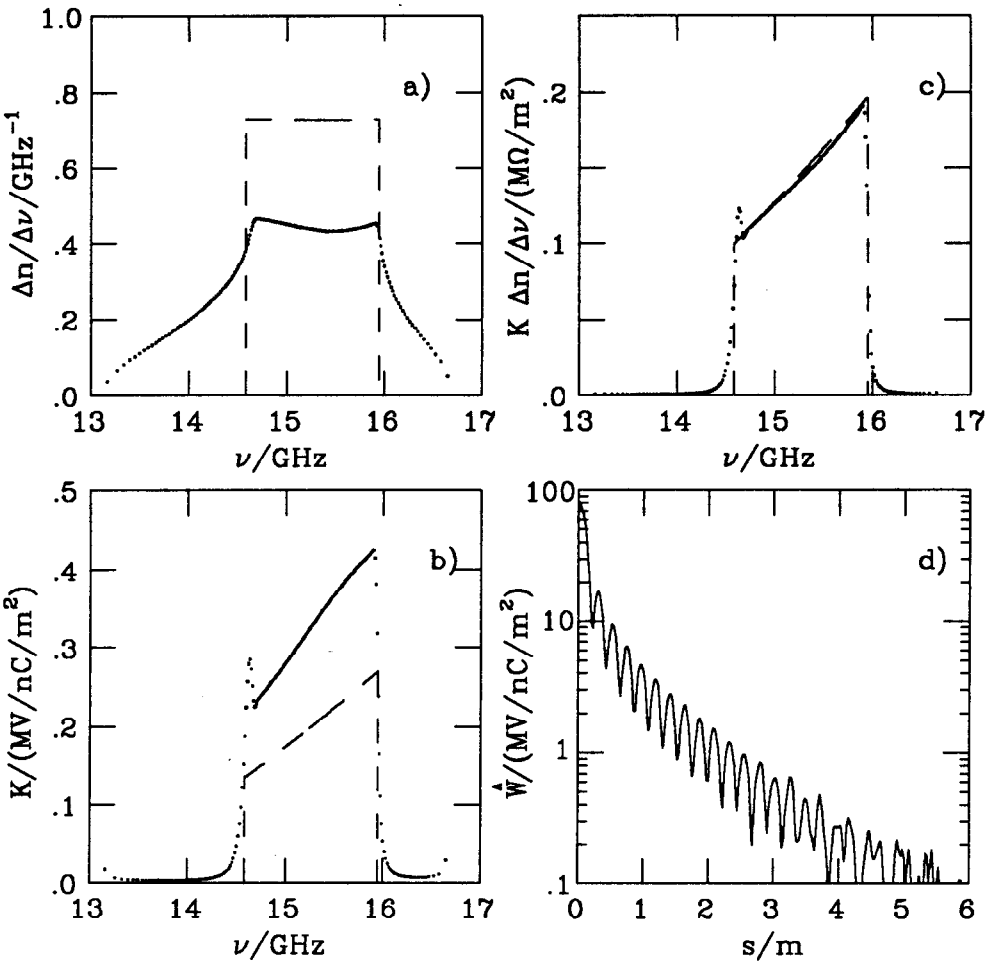

Fig. 10. The normal mode frequency distribution $\Delta n/\Delta\nu$ (a), the kick factors K (b), the product $K\,\Delta n/\Delta\nu$ (c) and the wakefield envelope $\hat{W}$ (d) for the single circuit chain model of the detuned structure. The distribution of ν_s is uniform with a full-width $\Delta\nu_s/\bar{\nu}_s = 9$ %. The dashes [in (a)-(c)] connect the uncoupled solutions.

frequency range. In frame (c) we see again that $K\Delta n/\Delta\nu$ is almost the same for the coupled as for the uncoupled calculation, and that the primary difference is in smoother tails. And in frame (d) we note that wakefield is almost the same as the one for the uncoupled calculation. The somewhat lower amplitude level in the interval $s = 0.7$ m and $s = 6$ m can be attributed to the smoother tails of $K\Delta n/\Delta\nu$. To test for the effects of the precursor voltage in the circuit (discussed

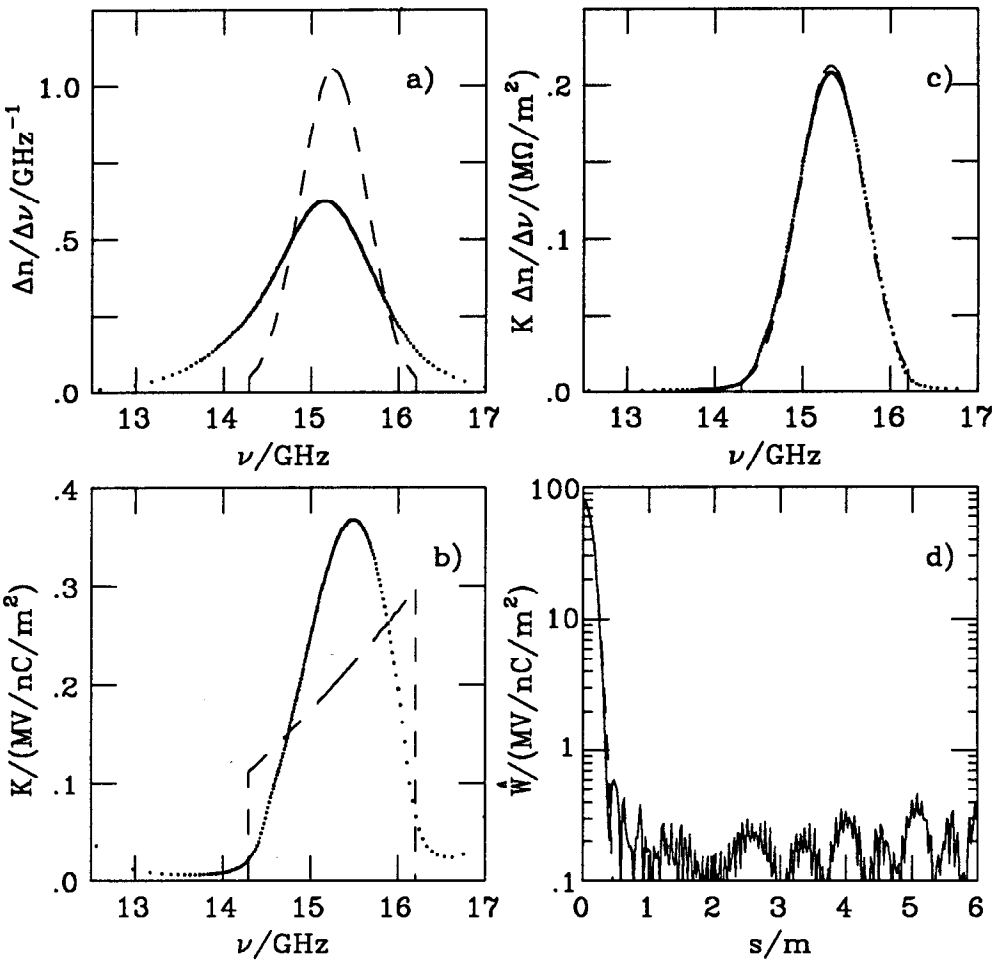

Fig. 11. The normal mode frequency distribution (a), the kick factors (b), the product $K\,\Delta n/\Delta\nu$ (c) and the wakefield envelope $\hat{W}$ (d) for the single circuit chain model of the detuned structure. The distribution of ν_s is Gaussian with $\sigma_{\nu_s}/\bar{\nu}_s = 2.5$ %. The dashes [in (a)-(c)] connect the uncoupled solutions.

in Sec. 2.3) we have repeated the wakefield calculation, but now using the more involved combination of Eqs. (2.42), (2.46), (2.47). We find that the difference in the results is negligible. Finally, in Fig. 12 we plot some mode patterns for this example. For modes p we display $V_m^{(p)}/(q_e x_e L)$ defined by Eq. (2.44). The range of the ordinates of the plots is ± 0.35 MV/nC/m^2. These plots, in addition to

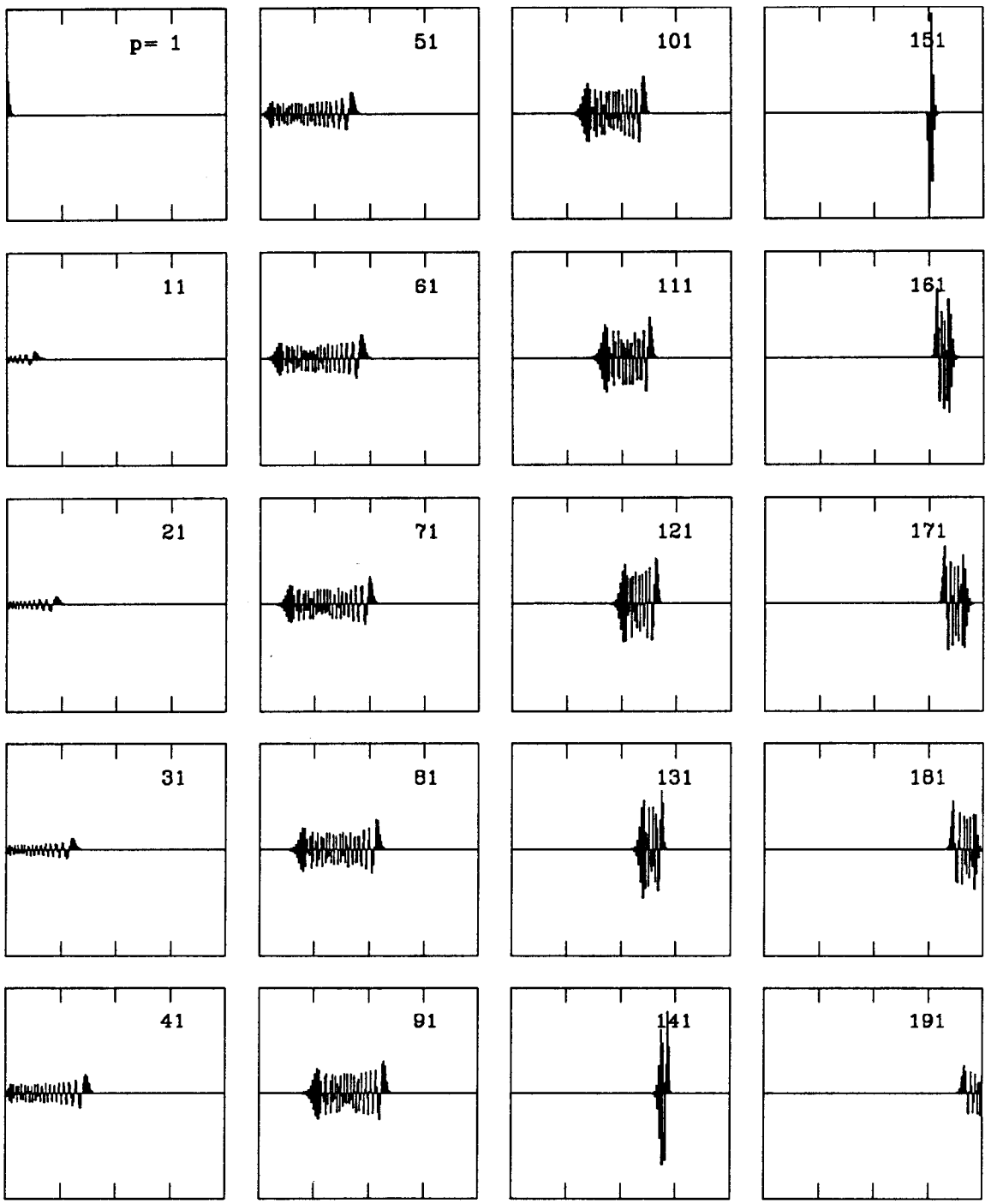

Fig. 12. Some mode patterns for the single band model. For modes p we display $V_m^{(p)}/(q_e x_e L)$ with a range ± 0.35 MV/nC/m^2. The abscissas give m from 0 to 200. The distribution in ν_s is Gaussian with $\sigma_{\nu_s}/\bar{\nu}_s = 2.5$ %.

showing the mode patterns, give the amplitudes at which the modes are excited by the driving charge.

To see the effect of the boundary conditions on the wakefield we have repeated our calculation for a Gaussian detuned cavity but now taking as boundary conditions Eq. (2.8), the boundary conditions corresponding to half-cells on the ends. We see that to 1% of the peak the wakefields have not changed. We therefore conclude that our results are not sensitive to the boundary conditions. This is consistent with our earlier observation that, for the NLC structure with its peculiar dispersion characteristics, those modes that touch the end walls have their loss factors greatly depressed.

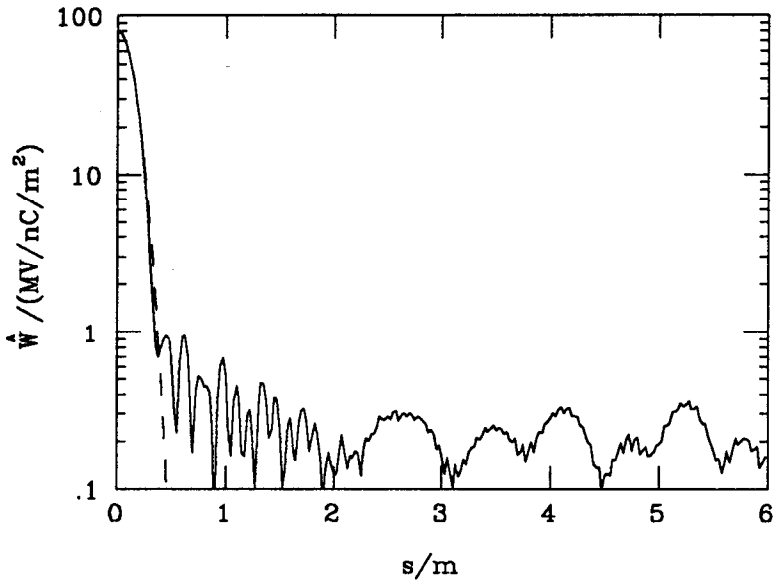

Fig. 13. The wakefield envelope for a Gaussian detuned structure with half-cells at the ends, corresponding to the boundary conditions of Eq. (2.8).

The results for the wakefield using a Gaussian distribution of cell parameters are encouraging. However, the use of a single circuit chain is not readily justified, particularly since it corresponds to dispersion curves which are not in good agreement with those obtained from TRANSVRS. In the next chapter we therefore

try to put the equivalent circuit on a more physical basis. This leads to a double circuit chain which fits the dispersion curves extremely well. At the same time, the wakefield predictions are not changed substantially, but now we can have greater confidence in the results.

2.5.1 Losses

Before proceeding to the next chapter let us give one example of a calculation including losses. It has been suggested that if we combine detuning of the structure with a relatively strong de-queueing of only a few cells we might be able to reduce the wake at even longer distances than just detuning alone would. To test this principle we detune our cavity as a Gaussian as before; in addition we now de-queue five cells to $Q_m = 1000$, while setting the rest of them to $Q_m = 6500$. The first detuned cell is number 20, and the spacing between detuned cells is 40 cells. The resulting normal mode Q's, obtained using Eq. (2.55), are displayed in Fig. 14. We see that there is a great scatter in the Q's, and we expect that this will make the wakefield worse rather than better at long distances. Note that for this example the maximum of the $c_{qp}/|f^{(p)}|$, the parameter that needs to be small for the perturbation calculation to be valid, was found to be around 0.1. Roughly this size occurred in 5 instances; for most elements it was $\lesssim 0.025$. We, therefore, expect the results of this perturbation calculation to be valid.

3. Double Chain of Coupled Circuits

3.1 The Difference Equations

In an effort to put the difference equations corresponding to the equivalent circuit on a more physical basis we expand the fields in each cell into an infinite set of orthonormal modes and relate the coefficients in adjacent cells to one another by treating the iris coupling using the static approximation of Bethe.[19] The details are presented in the Appendix. In the present application we assume that the only

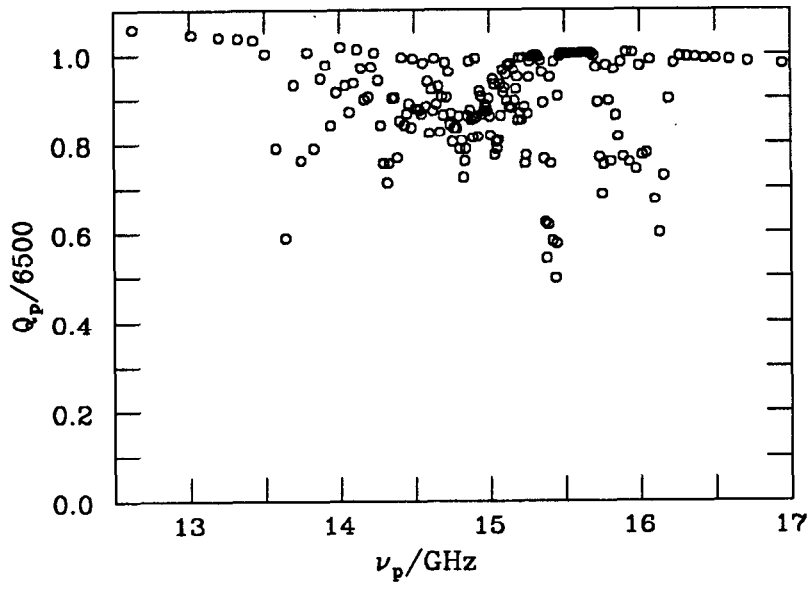

Fig. 14. The normal mode Q's for our de-queueing example. The modes are detuned according to a Gaussian distribution, with $\sigma_{\nu_s}/\bar{\nu}_s = 2.5$ %.

cell modes of importance are the TM_{110} and the TE_{111} modes with coefficients f_m and $\hat{f}_m$ in each cell, and obtain the difference equations [Eqs. (A.18), (A.19)]

$$(x_m-\lambda)f_m-\frac{\kappa_{m+\frac{1}{2}}}{2}f_{m+1}-\frac{\kappa_{m-\frac{1}{2}}}{2}f_{m-1}=-\frac{\sqrt{\kappa_{m+\frac{1}{2}}\hat{\kappa}_{m+\frac{1}{2}}}}{2}\hat{f}_{m+1}+\frac{\sqrt{\kappa_{m-\frac{1}{2}}\hat{\kappa}_{m-\frac{1}{2}}}}{2}\hat{f}_{m-1} \tag{3.1}$$

$$(\hat{x}_m-\lambda)\hat{f}_m+\frac{\hat{\kappa}_{m+\frac{1}{2}}}{2}\hat{f}_{m+1}+\frac{\hat{\kappa}_{m-\frac{1}{2}}}{2}\hat{f}_{m-1}=\frac{\sqrt{\kappa_{m+\frac{1}{2}}\hat{\kappa}_{m+\frac{1}{2}}}}{2}f_{m+1}-\frac{\sqrt{\kappa_{m-\frac{1}{2}}\hat{\kappa}_{m-\frac{1}{2}}}}{2}f_{m-1}\,. \tag{3.2}$$

The definitions of the parameters x_m, $\hat{x}_m$, $\kappa_{m\pm\frac{1}{2}}$, $\hat{\kappa}_{m\pm\frac{1}{2}}$, are given in Eqs. (A.20), (A.21), in terms of properties of the TM_{110} and the TE_{111} modes and of the susceptibilities of the iris holes. However, as described below, instead of using these relations to find the parameters we will obtain them by fitting the dispersion curves obtained by TRANSVRS. Note that if our cavity contains N cells then Eqs. (3.1), (3.2), represent a symmetric eigenvalue problem with $2N$ eigenvalues and $2N$ eigenfunctions. An equivalent circuit representation of Eqs. (3.1), (3.2), with the cell frequencies given by $\nu_m = 1/\sqrt{x_m}$ and $\hat{\nu}_m = 1/\sqrt{\hat{x}_m}$, is sketched in

Fig. 15. Note that with the cross-coupling terms set to zero Eqs. (3.1), (3.2), are of the same form as the single circuit chain equation Eq. (2.4). However, unlike in the earlier equation the coupling coefficients in Eqs. (3.1), (3.2), represent only positive quantities; the signs in front of the coupling terms reflect the fact that with magnetic coupling a TM mode is a backward wave and a TE mode is a forward wave.

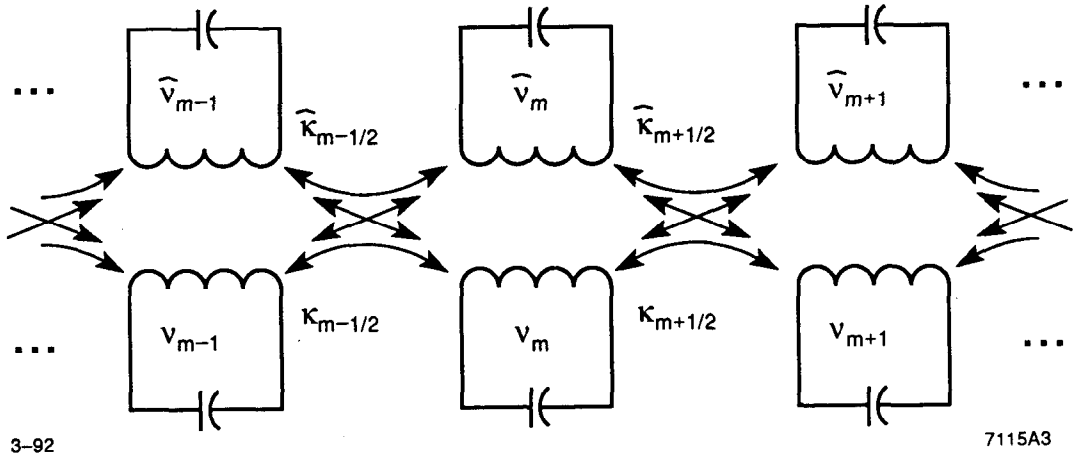

Fig. 15. An equivalent circuit representation of Eqs. (3.1), (3.2).

Just as in the single circuit chain model several choices of boundary condition are possible. If we assume that the cavity consists of N full cells ($m = 1, 2, \ldots, N$), with metallic end walls, the boundary conditions correspond to

$$\begin{aligned} f_0 = f_1\ , \quad \hat{f}_0 = -\hat{f}_1\ , \quad \kappa_{\frac{1}{2}} = \kappa_1\ , \quad \hat{\kappa}_{\frac{1}{2}} = \hat{\kappa}_1 \quad , \\ f_{N+1} = f_N\ , \quad \hat{f}_{N+1} = -\hat{f}_N\ , \quad \kappa_{N+\frac{1}{2}} = \kappa_N\ , \quad \hat{\kappa}_{N+\frac{1}{2}} = \hat{\kappa}_N \quad . \end{aligned} \tag{3.3}$$

If we assume $N-2$ full cells ($m = 2, 3, \ldots, N-1$) with two half cells ($m = 1$, N) with metallic end walls, the boundary conditions correspond to

$$\begin{aligned} f_0 = f_2\ , \quad \hat{f}_0 = 0\ , \quad \kappa_{\frac{1}{2}} = \kappa_{\frac{3}{2}}\ , \quad \hat{\kappa}_{\frac{1}{2}} = \hat{\kappa}_{\frac{3}{2}} \quad , \\ f_{N+1} = f_{N-1}\ , \quad \hat{f}_N = 0\ , \quad \kappa_{N+\frac{1}{2}} = \kappa_{N-\frac{1}{2}}\ , \quad \hat{\kappa}_{N+\frac{1}{2}} = \hat{\kappa}_{N-\frac{1}{2}} \quad . \end{aligned} \tag{3.4}$$

The dispersion curves for the periodic structure corresponding to our two chain model are easily obtained by setting

$$f_m = f \cos m\phi \quad \text{and} \quad \hat{f}_m = \hat{f} \sin m\phi \tag{3.5}$$

in Eqs. (3.1), (3.2), and treating all other parameters as independent of m. We then obtain

$$(x - \lambda - \kappa \cos\phi) f = -\sqrt{\kappa\hat{\kappa}} \sin\phi \, \hat{f} \quad , \tag{3.6}$$

$$(\hat{x} - \lambda + \hat{\kappa} \cos\phi) \hat{f} = -\sqrt{\kappa\hat{\kappa}} \sin\phi \, f \quad . \tag{3.7}$$

Combining these equations we obtain the dispersion relation:

$$\cos\phi = \frac{\kappa\hat{\kappa} - (x - \lambda)(\hat{x} - \lambda)}{(x - \lambda)\hat{\kappa} - (\hat{x} - \lambda)\kappa} \quad . \tag{3.8}$$

When plotted as $\cos\phi$ against λ, Eq. (3.8) is a hyperbola with asymptotes

$$\lambda = \frac{x\hat{\kappa} - \hat{x}\kappa}{\hat{\kappa} - k} \equiv \lambda_0 \quad \text{and} \quad \cos\phi = \lambda - \frac{\hat{x}\hat{\kappa} - x\kappa}{(\hat{\kappa} - \kappa)^2} \quad . \tag{3.9}$$

If our model is realistic, the two dispersion curves in Fig. 3 marked C, D, or E should therefore be part of the branches of a hyperbola with one horizontal asymptote, and they are. The frequencies of the zero and pi modes of the two bands for C, D, or E are given by

$$\lambda_0^{(1,2)} = x - \kappa \, , \; \hat{x} + \hat{\kappa} \quad \text{and} \quad \lambda_\pi^{(1,2)} = x + \kappa \, , \; \hat{x} - \hat{\kappa} \tag{3.10}$$

and the four parameters x, $\hat{x}$, κ, $\hat{\kappa}$ can be obtained directly from $\lambda_0^{(1,2)}$, $\lambda_\pi^{(1,2)}$ [with some ambiguity as to which band corresponds to (1) or (2)]. We have obtained the zero and pi mode frequencies for the geometries A-G using TRANSVRS and then by the above procedure have found the four needed parameters as functions of iris radius a. The results are shown in Fig. 16. Substituting these parameters

into our difference equations we obtain, for periodic structures with the geometries A-G, the dispersion curves shown in Fig. 17. The agreement with the TRANSVRS dispersion curves is far better than that from the single band fit and is excellent, except for some small departure in the upper band where the iris radius is largest, most likely due to the neglected frequency dependence of the coupling and/or the neglect of still higher cell modes. It should be noted that neither κ nor $\hat{\kappa}$ change sign when going from C to D to E. However the opposite sign of κ and $\hat{\kappa}$ on the left side of Eqs. (3.6) and (3.7) apparently plays the role of a sign change in the coupling when the mode changes its TM_{110}/TE_{111} mix as one proceeds down the tapered structure.

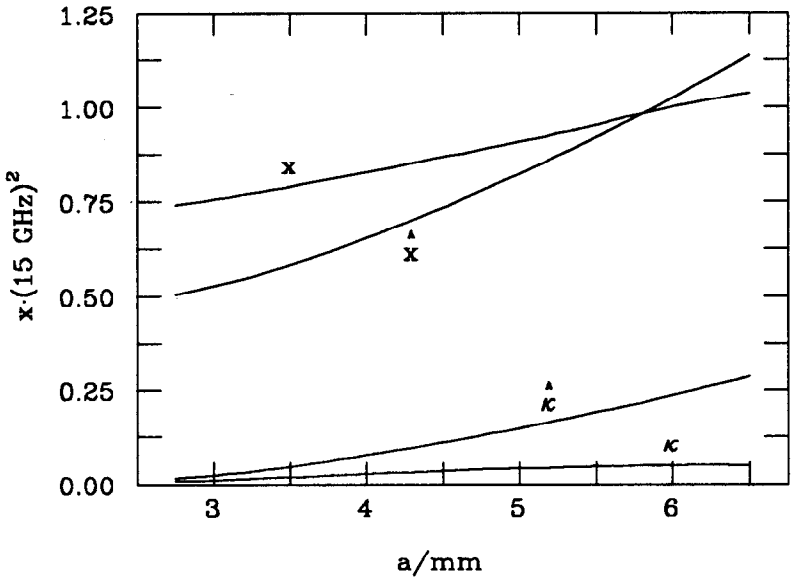

Fig. 16. The two-band parameters x, $\hat{x}$, κ, $\hat{\kappa}$ as functions of iris radius a for periodic geometries A-G.

For example, let us construct $1+\cos\phi$ from Eq. (3.8) since we are most interested in the modes near $\phi = \pi$ for our structure. We find

$$1+\cos\phi = \frac{(\lambda-\lambda_\pi^{(2)})(\lambda_\pi^{(1)}-\lambda)}{(\hat{\kappa}-\kappa)(\lambda_0-\lambda)} \tag{3.11}$$

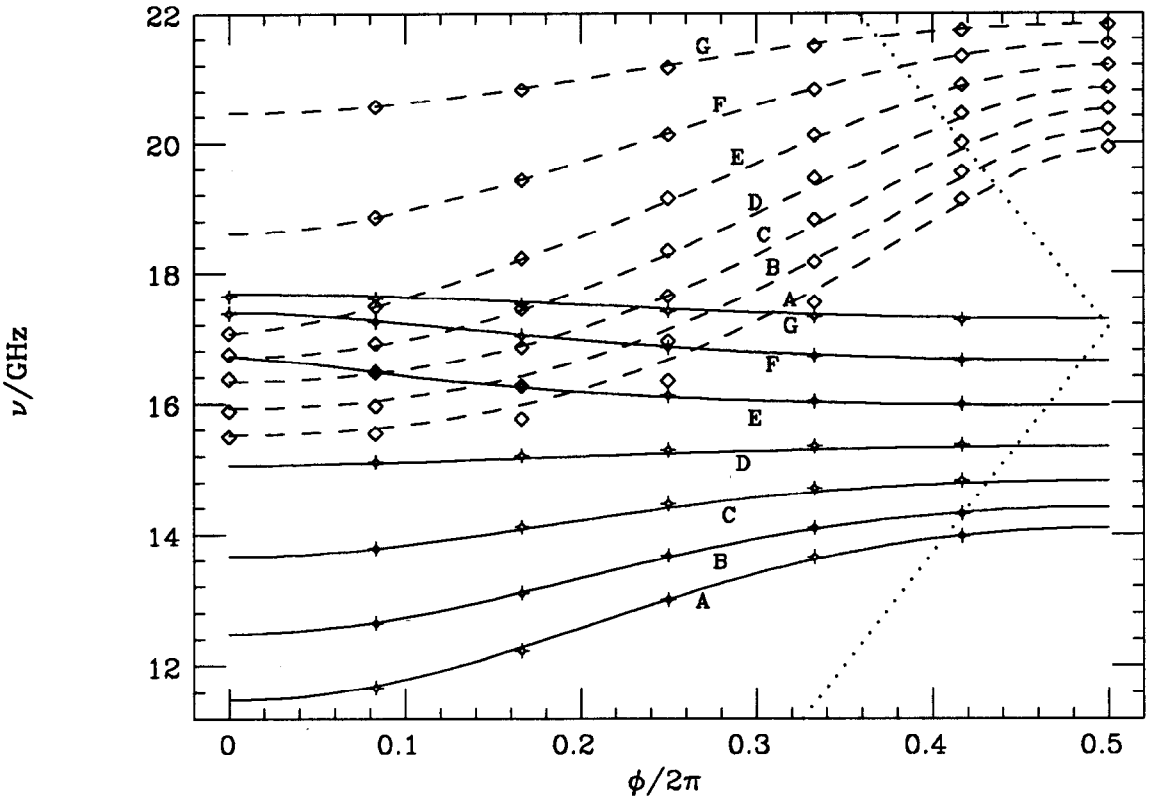

Fig. 17. The double circuit chain solutions for a structure with 6 identical cells (the plotting symbols). Results are given for cell geometries *A*-*G*. The crosses represent modes belonging to the 1st band, the diamonds those of the 2nd band. For comparison, the dispersion curves obtained from TRANSVRS are also shown. The dots give the speed of light line.

Near $\phi = \pi$,

$$1 + \cos\phi = \frac{(\phi - \pi)^2}{2} \tag{3.12}$$

and the factor $1 + \cos\phi$ plays the role of

$$-\frac{1}{2f}\frac{d^2 f}{dm^2}$$

in Eq. (2.28). Equations (3.6), (3.7) therefore correspond approximately to the single band equation

$$\frac{d^2f}{dm^2} + \frac{2(\lambda - \lambda_\pi^{(2)})(\lambda - \lambda_\pi^{(1)})}{(\hat{\kappa} - \kappa)(\lambda_0 - \lambda)} f \cong 0 \quad . \tag{3.13}$$

If $\lambda_\pi^{(1)}$ and λ_0 are close to one another, and distant from $\lambda_\pi^{(2)}$, as is the case near where the lower band goes from forward to backward wave, the eigenvalues λ_p will be near λ_0 and $\lambda_\pi^{(1)}$, and we can approximate $\lambda - \lambda_\pi^{(2)}$ by $\lambda_\pi^{(1)} - \lambda_\pi^{(2)}$. Thus we have

$$\frac{d^2f}{dm^2} + \frac{2(\lambda_\pi^{(1)} - \lambda_\pi^{(2)})(\lambda - \lambda_\pi^{(1)})}{(\hat{\kappa} - \kappa)(\lambda_0 - \lambda)} f \cong 0 \quad , \tag{3.14}$$

in which the vanishing of the denominator in the second term corresponds to the vanishing of $\kappa(m)$ in the single chain model, Eq. (2.28), at some cell within the cavity.

3.2 The Kick Factors

The derivations of the time development of the fields, the wakefields, and the kick factors for the double-band circuit model proceed in a fashion similar to the corresponding derivations for the single-band circuit model given in Sec. 2.3, and the form of the results is also similar. As before, we again fit to the kick factor for a periodic structure K_s, obtained using the computer program TRANSVRS. The kick factor for the double-band model is given by

$$K_p = \frac{|\sum_n f_n^{(p)} \sqrt{\epsilon^{(n)} K_s^{(n)} \nu_s^{(n)}} e^{in\varphi_p}|^2}{N\nu_p[|f^{(p)}|^2 + |\hat{f}^{(p)}|^2]} \quad , \tag{3.15}$$

with $\epsilon^{(m)}$ a fitting parameter and again $\varphi_p = 2\pi\nu_p L/c$ the phase shift per cell. Note that only the f_m's appear in the numerator of the above expression, since only the TM_{110} component of the fields (and not the TE_{111} component) will kick the beam. We obtain the fitting parameter by running our circuit program for a multi-loop, periodic circuit. Then ϵ is given by $1 + |\hat{f}^{(p)}|^2/|f^{(p)}|^2$, where p is the mode nearest the synchronous point.

In an infinitely periodic structure the beam will, on average, only interact with a mode that has a phase velocity synchronous with the beam. For a mode with a non-synchronous phase velocity the beam will lose energy in some cells, gain energy in others, but on average have no interaction. However, even for a non-synchronous mode we can calculate an interaction factor $\tilde{K}_s$ which gives the maximum kick a particle can receive in one cell of a periodic structure, using TRANSVRS. This parameter is a measure of the field properties for a non-synchronous phase advance; at the synchronous phase it equals K_s. The factor $\tilde{K}_s$ for the lowest dipole band for cell geometries C-E, as obtained by TRANSVRS, is plotted as function of phase advance in Fig. 18. (Note that the period of this function is 2π, and we plot only one-half the period.) We note that near pi phase advance, near the synchronous phase, $\tilde{K}_s$ is large and near zero phase advance this parameter becomes small. This behavior signifies that the mode is largely TM-like near pi phase advance and TE-like near zero. (Although not shown, the next band behaves in a complementary way: it is TM-like near zero phase advance and TE-like near pi, near the synchronous phase.)

By solving a periodic circuit with our two-band program we can see how well our expansion of the fields in terms of the TM_{110} and the TE_{111} modes approximates the hybrid fields in a real, periodic cavity. For our two-band program the single cell kick factor for mode p is given by

$$\tilde{K}_s = \frac{|f^{(p)}|^2 \epsilon K_s \nu_s}{|f^{(p)}|^2 + |\hat{f}^{(p)}|^2} \quad . \tag{3.16}$$

The results of the program, for periodic structures with geometries C-E, are given by the dots in Fig. 18. We see that the results of the model behave only roughly in the correct way. One clear difference is that the slope of $\tilde{K}_s$ for the model is zero at $\phi = \pi$, whereas this is not the case for the real cavity. The discrepancy in the dependence of $\tilde{K}_s$ on ϕ shows a limitation of our model; however, this discrepancy is not terribly important for our purposes, since the contribution of the non-synchronous modes to the total kick factor of an N-cell structure will be

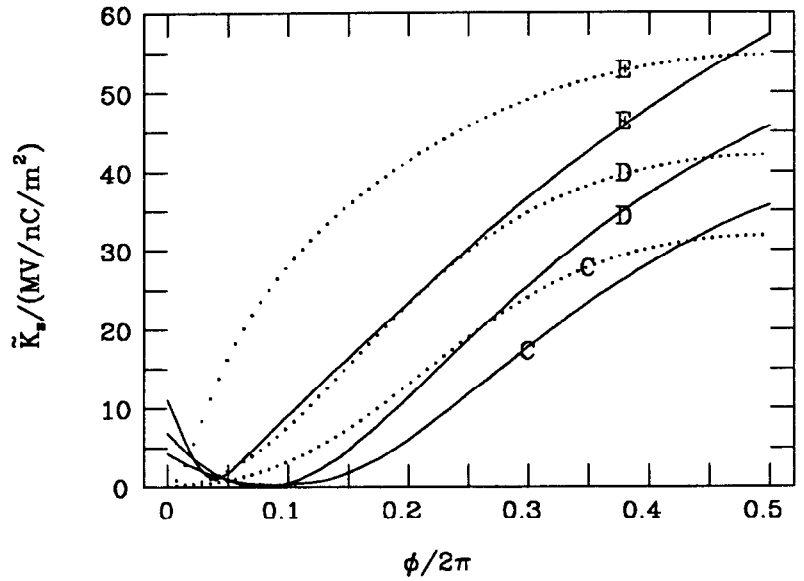

Fig. 18. The single cell kick factor $\tilde{K}_s$ for a periodic structure with dimensions C, D, and E, as function of phase advance per cell. The solid curves give results obtained by TRANSVRS, the dots give those obtained by the two band circuit calculation.

down on the order of $1/N$ as compared to that of the synchronous modes. Finally note that the single band model gives even worse agreement; it results in only horizontal lines for $\tilde{K}_s$ as function of ϕ.

3.3 Simulation Results

We have written a computer program that solves Eqs. (3.1), (3.2), to find the eigenmodes of the double-band circuit model of the tapered structure. Like for the single band program we first find the constants in the equations x_m, $\hat{x}_m$, κ_m, $\hat{\kappa}_m$, for the cell geometries A-G using TRANSVRS, and then find them for any intermediate cell geometry by cubic spline interpolation. After having solved for the eigenmodes of a tapered structure we obtain the kick factors using Eq. (3.15). And, if desired, the Q's of the modes can be found in a fashion similar to that described in Section 2.4 for the single band model.

The results for our Gaussian detuned, NLC cavity, using the two band model are shown in Figs. 19-22. In Fig. 19 we show the mode spectrum, kick factor, kick factor times mode density, and wake function up to 17 GHz. We focus on the modes belonging to the first band since the contribution of the second band modes to the wakefield itself is negligible and can be ignored. In Fig. 19a we see that the peak of the frequency distribution is only 1.4 times the uncoupled calculation, rather than the 1.7 factor obtained from the single band model. Some of the 2nd band modes can be seen as the beginnings of a second peak at higher frequencies. In panel (b) we note that the kick factors of these 2nd band modes are very small (they can barely be seen). As to the results of the first band modes we note from panels (a)-(d) that, although there are some differences, these results are rather similar to the results of the single-band model (compare Fig. 11). In particular, the wakefields are quite close to the wakefields obtained with the simpler model.

In Fig. 20 we show some mode patterns for modes of the first band; for modes p we display $V_m^{(p)}/(q_e x_e L)$ which is given by the two-band correspondent of Eq. (2.44). The extent of the modes is similar as for the single band model but there are some differences in the details of the mode shapes (compare Fig. 12). In Fig. 21 we plot the kick profile $\tilde{V}_m$ experienced by a test particle a quarter wavelength ($s = 2$ mm) behind the driving charge. This is the position of maximum total kick (at $s = 0$ the result is zero since the driving bunch does not kick itself transversely). Note that the kick continually increases as the test particle traverses the cavity, due to the ever decreasing size of the irises. The area under this curve 80 MV/nC/m^2 gives the wakefield at $s = 2$ mm. And finally in Fig. 22 we display the kick profiles seen by the nine bunches, each separated by 42 cm, that follow the driving bunch in the NLC bunch train. We see that for all the trailing bunches the kick patterns describe sinusoidal oscillations that extend almost over the entire cavity length.

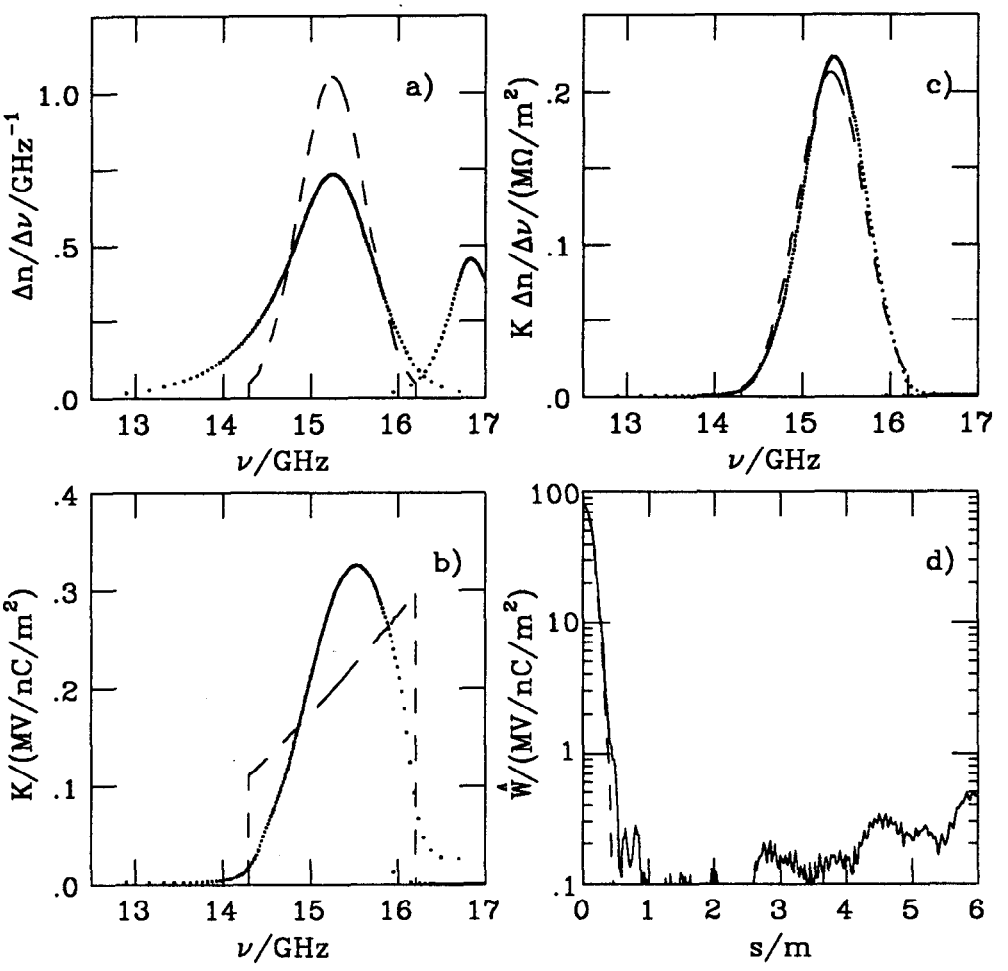

Fig. 19. Part of the normal mode frequency distribution (a), the kick factors (b), the product $K\,\Delta n/\Delta\nu$ (c), and the wakefield envelope $\hat{W}$ (d) for the double circuit chain model of the detuned structure. The distribution of ν_s is Gaussian with $\sigma_{\nu_s}/\bar{\nu}_s = 2.5$ %. The dashes [in (a)-(c)] connect the uncoupled solutions.

4. Conclusions

In this paper we have studied the normal modes (in the first dipole passband) of a detuned, X-band accelerator structure, a structure that has been proposed for the Next Linear Collider. A unique feature of our cavity is that the equivalent cell-to-cell coupling changes sign somewhere within the structure. We present two

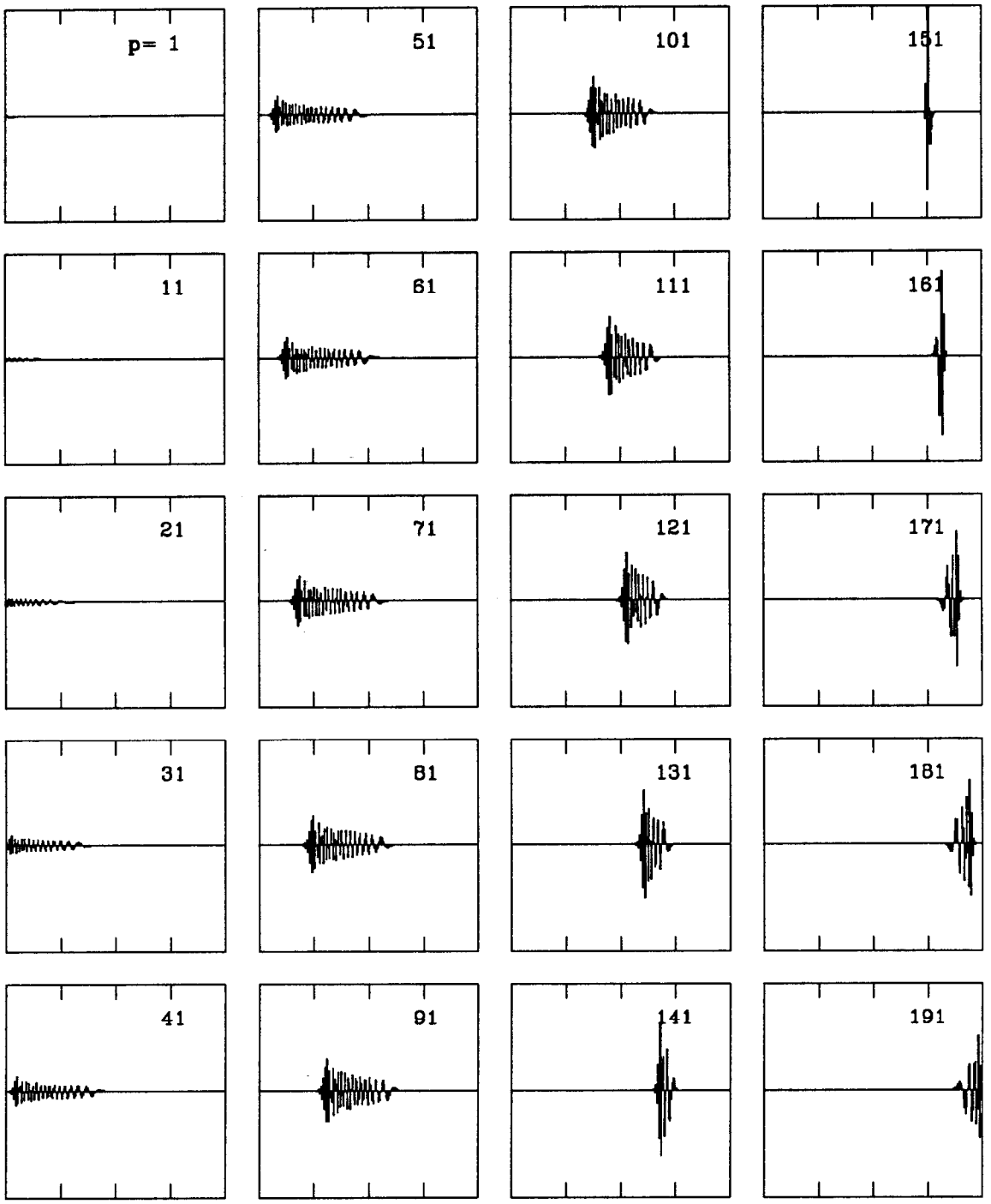

Fig. 20. Some mode patterns for the double band model. For modes p we display $V_m^{(p)}/(q_e x_e L)$ with a range ± 0.35 MV/nC/m^2. The abscissas give m from 0 to 200. The distribution in ν_s is Gaussian with $\sigma_{\nu_s}/\bar{\nu}_s = 2.5$ %.

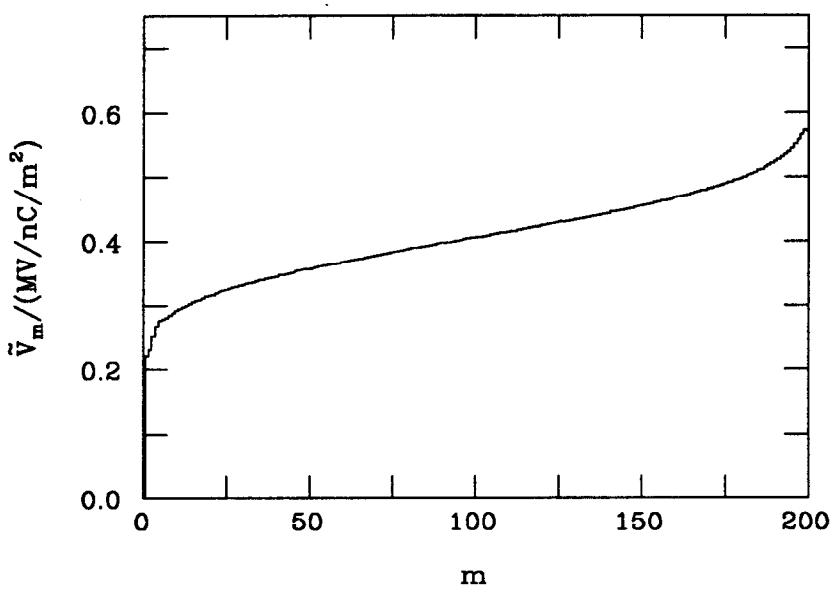

Fig. 21. The transverse kick profile $\tilde{V}_m$ seen by a test particle following behind the driving charge at $s = 5$ mm.

equivalent circuit models that can be applied to finding the modes in this cavity. We find the eigenfunctions of these circuit models using a matrix method, and from the results we obtain the frequencies, the kick factors, and the quality factors of the cavity modes. These, in turn, give us the wakefields for all positions.

The first circuit model that we introduce consists of a single chain of resonators and the second one of a double chain of resonators. The second model includes the effects of the second passband modes on the properties of the first. It is a model that we derive from the properties of Maxwell's equations at an iris, and it assumes that the fields in the cavity can be approximated by a simple combination of a TM_{110} and a TE_{111} mode. We find that the change of sign of the coupling in our detuned cavity can be explained as a change in the make-up of this combination as the cell geometry changes.

The elements of the circuits are found by fitting to the dispersion curves and the synchronous kick factor obtained from TRANSVRS, a computer program that solves Maxwell's equations in a periodic structure. We find that both circuit mod-

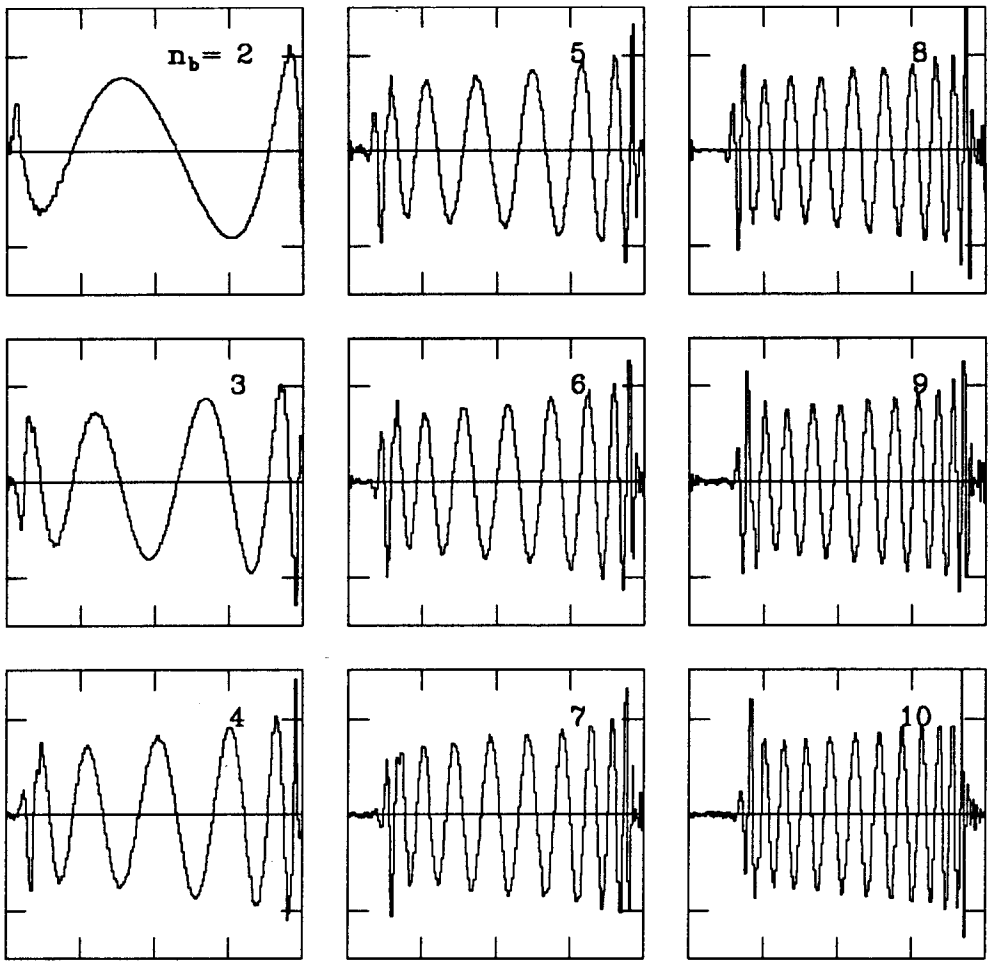

Fig. 22. The transverse kick profile $\tilde{V}_m$ due to bunch number $n_b = 1$ experienced by the following bunches. The bunch separation is 42 cm. The ordinate range is ± 0.75 MV/nC/m^2. The abscissas give m from 0 to 200.

els, but particularly the two-band model, when applied to a periodic cavity, give dispersion curves that agree well with those obtained by TRANSVRS. However, the dependence of the single cell kick factor on phase advance is completely wrong for the single band model, and only in rough agreement for the double band model, when compared with TRANSVRS results. This indicates that the make-up of the fields is not as simple as our two models assume. However, the effect of this discrepancy on the kick factors of a many-cell cavity should be small, since a beam

interacts strongly only with waves with a phase velocity that is very close to c, and these are the waves for which the fit parameter of the model is adjusted. The above two observations lead us to believe that for the detuned structure: (i) the normal mode frequencies are accurate and (ii) the normal mode kick factors are also accurate, except in the tails of the distribution. Consequently, we believe that the wakefield is also accurate. As evidence of this we note that the wakefields obtained using the two models, over the interval of interest to us, agree to good accuracy.

It has been proposed to operate the NLC with 10 bunches in a train. Earlier calculations for the NLC that did not consider the cell-to-cell coupling in the cavity found that by detuning the cells according to the proper Gaussian distribution the amplitude of the wakefield at the positions of the trailing bunches was sufficiently small to avoid the multi-bunch instability. The results of the calculations using either of our two models agree with the earlier results and with the conclusion.

Other observations: (i) The frequency distribution of the modes is broader than that assumed by the earlier calculation. Effects of this on the wakefield will only become evident at longer distances, $c \sim c/\delta\nu$ with $\delta\nu$ the typical spacing of modes. (ii) The difference equations for a single chain can be approximated by a differential equation which has an exact solution that predicts that the modes are localized between the cell in which the coupling changes sign and the cell whose resonant frequency is that of the mode in question. (iii) This conclusion is also borne out by the numerical solutions to the difference equation which show that most modes are localized and do not reach the ends of the cavity. In fact the modes which do reach the ends interact only weakly with the beam. Therefore the boundary conditions do not have much of an effect on the wakefield. (iv) Combining detuning of the cavity with de-queueing a small number of cells will probably result in a worse long-range wakefield than if de-queuing were not used at all.

The results of this paper indicate that detuning the cavity by varying the iris radii of the cells sufficiently cancels the wakefield for NLC requirements. But

here we have only investigated the effects of the first (or at most the first two) dipole bands. When we study the effects of the higher band modes we find that their contribution—even for the detuned cavity—is not, in fact, sufficiently small. The cure for this, we find, is to vary the iris thicknesses, as well as the iris radii, according to a Gaussian distribution as one moves along the structure. This topic will be the subject of a future paper.

Acknowledgments

The authors thank N. Holtkamp for getting us started in the equivalent circuit approach to detuned cavities. One of us (K. B.) also thanks M. Sands for many helpful discussions, particularly concerning the circuit model, and R. Warnock, for discussions about mathematical techniques. We have also greatly profited from discussions at the weekly Structures Meeting at SLAC, where these results were first presented, and thank all the members of the group.

REFERENCES

1. B. Richter, Proceedings of the Workshop on Physics and Experiments with Linear Colliders, Saariselka, Finland, Sept. 1991, and SLAC PUB-5736, Feb. 1992.
2. H. Deruyter, *et.al.*, Proceedings of the 1989 Particle Accelerator Conf., Chicago, IL., p. 156, 1989.
3. H. Deruyter, *et.al.*, Proceedings of the 1990 Linear Accelerator Conf., Albuquerque, NM., p. 132, 1990.
4. R. Ruth, Proceedings of the Workshop on Physics and Experiments with Linear Colliders, Saariselka, Finland, Sept. 1991, and SLAC PUB-5729, Mar. 1992.
5. K.A. Thompson, private communication.
6. K.A. Thompson and J.W. Wang, Proceedings of the 1991 IEEE Particle Accelerator Conf., San Francisco, CA., p. 431, 1991.

7. T.I. Smith, HEPL 437, Stanford University, 1966.

8. D.E. Nagle, *et.al.*, *Rev. Sci. Instrum.*, **38**, 1583 (1967).

9. J. Rees, PEP Note 255, SLAC, 1976.

10. M. Drevlak, *Dämpfung von transversalen Moden durch variable Zellgeometrieen in Wanderwellenröhren*, Thesis, Technische Hochschule Darmstadt, Darmstadt, Germany, Dec. 1991.

11. K. Bane and N. Holtkamp, SLAC-AAS-63, Sept. 1991.

12. R. Miller, oral presentation at the ICFA Workshop on Linear Colliders, Protvino, Russia, Sept. 1991.

13. M. Yamamoto, *et.al.*, KEK-PREPRINT-91-153, Nov. 1991.

14. K. Bane and B. Zotter, Proceedings of the 11^{th} Int. Conf. on High Energy Accelerators, CERN (Birhäuser Verlag, Basel, 1980), p. 581.

15. K. Bane, T. Weiland, P.B. Wilson, in *Physics of High Energy Particle Accelerators*, AIP Conf. Proc. No. 127, (Am. Inst. of Physics, New York, 1983).

16. J. Mathews and R. Walker, *Mathematical Methods of Physics*, 2^{nd} Edition, (W.A. Benjamin, Inc., New York, 1970), Chaps. 9-10.

17. W. Panofsky and W. Wenzel, *Rev. Sci. Instrum.* **27**, 967 (1956).

18. T. Weiland, *Nucl. Instrum. and Methods* **216**, 329 (1983).

19. H.A. Bethe, *Phys. Rev.* **66**, 163 (1944).

20. R. L. Gluckstern and J. A. Diamond, *IEEE Transactions on Microwave Theory and Techniques* **39**, No. 2, 274 (1991).

APPENDIX
Circuit Chains from Maxwell's Equations

We here derive the equations which connect the amplitude of the cell modes between adjacent cavities. The coupling arises from the penetration of the fields through the iris holes whose radius we assume is small compared to the wavelength, thereby permitting us to use a static approximation for the penetration. Moreover the coupling will be essentially magnetic since E_z vanishes at the center of the hole for all transverse modes.

The orthonormal modes are derived for a cell without iris holes. They are denoted by $\mathbf{e}_\ell$, $\mathbf{h}_\ell$ which satisfy

$$\nabla \times \mathbf{e}_\ell = k_\ell \mathbf{h}_\ell \quad , \qquad \nabla \times \mathbf{h}_\ell = k_\ell \mathbf{e}_\ell \quad , \tag{A.1}$$

with

$$\int \mathbf{e}_\ell \cdot \mathbf{e}_{\ell'} \, dv = \int \mathbf{h}_\ell \cdot \mathbf{h}_{\ell'} \, dv = \delta_{\ell\ell'} \quad , \tag{A.2}$$

and where $\mathbf{n} \times \mathbf{e}_\ell = 0$ and $\mathbf{n} \cdot \mathbf{h}_\ell = 0$ on the boundary. The actual fields are expanded in terms of these modes, with coefficients which play the role of voltages and currents. Specifically, we write

$$\mathbf{E}(\mathbf{x}) = \sum_\ell V_\ell \mathbf{e}_\ell(\mathbf{x}) \quad , \qquad \mathbf{H}(\mathbf{x}) = \sum_\ell I_\ell \mathbf{h}_\ell(\mathbf{x}) \quad , \tag{A.3}$$

with

$$V_\ell = \int \mathbf{E}(\mathbf{x}) \cdot \mathbf{e}_\ell(\mathbf{x}) \, dv \quad , \qquad I_\ell = \int \mathbf{H}(\mathbf{x}) \cdot \mathbf{h}_\ell(\mathbf{x}) \, dv \quad . \tag{A.4}$$

Note that Eq. (A.3) *cannot* be used directly to evaluate the transverse electric or longitudinal magnetic fields within the iris since these vanish in the individual terms. However it *can* be used to find the longitudinal electric and transverse magnetic fields within the iris which will form the starting point for electrostatic and magnetostatic calculations in the vicinity of the hole.

We now write Maxwell's Equations as

$$\nabla \times \mathbf{E} = -jkZ_0\mathbf{H} \quad , \quad Z_0\nabla \times \mathbf{H} = jk\mathbf{E} \quad . \tag{A.5}$$

Multiplying the first of Eqs. (A.5) by $\mathbf{h}_\ell$ and integrating over the cell volume, we find

$$\int dv\, \mathbf{h}_\ell \cdot \nabla \times \mathbf{E} = -jkZ_0 \int \mathbf{H} \cdot \mathbf{h}_\ell\, dv = -jkZ_0 I_\ell \quad . \tag{A.6}$$

Using $\nabla \cdot \mathbf{A} \times \mathbf{B} = \mathbf{B} \cdot \nabla \times \mathbf{A} - \mathbf{A} \cdot \nabla \times \mathbf{B}$, we find

$$k_\ell V_\ell + \int dS\, \mathbf{n} \cdot \mathbf{E} \times \mathbf{h}_\ell = -jkZ_0 I_\ell \quad . \tag{A.7}$$

Multiplying the second of Eqs. (A.5) by $\mathbf{e}_\ell$ and integrating over the cell volume similarly leads to

$$Z_0 k_\ell I_\ell = jkV_\ell \quad , \tag{A.8}$$

where $\int dS\, \mathbf{n} \cdot (\mathbf{e}_\ell \times \mathbf{H})$ vanishes since $\mathbf{n} \times \mathbf{e}_\ell = 0$ over the entire cell boundary. Combining Eqs. (A.7) and (A.8), we find for a particular cell

$$\left(k^2 - k_\ell^2\right) V_\ell = k_\ell \int dS\, \mathbf{n} \cdot \mathbf{E} \times \mathbf{h}_\ell \quad , \tag{A.9}$$

where the surface integral is now evaluated over the interior surface of the two iris holes in the cell.

As previously mentioned, the electric field at the center of the iris vanishes, and the coupling integral in Eq. (A.9) only has a magnetic contribution in lowest order of the hole radius. Specifically, for the iris configuration shown in Fig. 23 we have

$$\left(k^2 - k_\ell^2\right) V_\ell = -jkk_\ell Z_0 \left[h_{\ell x}(0) \int\int dxdy\; xH_z + h_{\ell y}(0) \int\int dxdy\; yH_z\right] \quad , \tag{A.10}$$

where $\mathbf{h}_\ell(0)$ is the constant tangential field on the dashed surfaces and where the surface integrals are over the dashed surfaces.

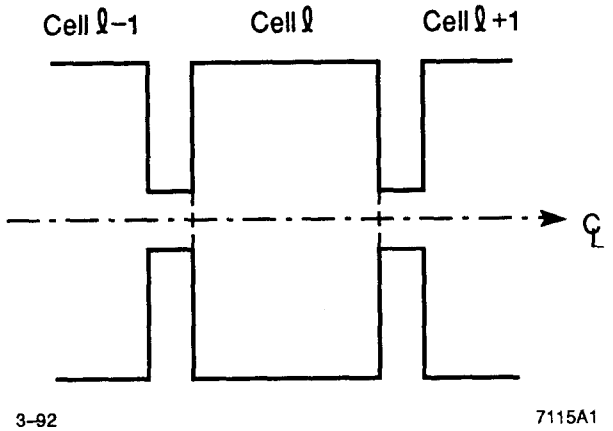

Fig. 23. The iris configuration.

For a thick wall the integrals in Eq. (A.10) can be written in terms of the "inside" and "outside" susceptibilities of the iris hole, and the tangential magnetic fields in the central cell and two adjacent cells.[20] Specifically, the double integrals can be written as

$$\int\int dxdy\,(\mathrm{i}x,\mathrm{j}y)\,H_z = \frac{\psi_{out}\mathbf{H}_+}{2} - \frac{\psi_{in}\mathbf{H}_-}{2} \quad , \tag{A.11}$$

where we have written only the contribution for the iris hole on the right in Fig. 23. Here $\psi_{out,in}$ are the "outside" and "inside" susceptibilities for the iris hole on the right, $\mathbf{H}_-$ is the tangential field on the right side of the central cell (with no iris hole) and $\mathbf{H}_+$ is the tangential field on the left side of the right adjacent cell.

Before proceeding further, we will assume that only two cell modes are important and denote them by $\mathbf{e}$, $\mathbf{h}$, k_m, V_m for the TM_{110} mode and $\hat{\mathbf{e}}$, $\hat{\mathbf{h}}$, $\hat{k}_m$, $\hat{V}_m$ for the TE_{111} mode. We shall also add a subscript m for cell m. Thus, Eq. (A.10) can be written as

$$\begin{aligned}(k^2 - k_m^2)\,V_m = -\frac{jkk_m}{2}Z_0 \Big[&\psi_{out}^{m+\frac{1}{2}}\,\mathbf{h}_m^+ \cdot \mathbf{H}_{m+1}^- + \psi_{out}^{m-\frac{1}{2}}\,\mathbf{h}_m^- \cdot \mathbf{H}_{m-1}^+ \\ &- \psi_{in}^{m+\frac{1}{2}}\,\mathbf{h}_m^+ \cdot \mathbf{H}_m^+ - \psi_{in}^{m-\frac{1}{2}}\,\mathbf{h}_m^- \cdot \mathbf{H}_m^-\Big] \quad ,\end{aligned} \tag{A.12}$$

and

$$\left(k^2 - \hat{k}_m^2\right) \hat{V}_m = -\frac{jk\hat{k}_m}{2} Z_0 \left[\psi_{out}^{m+\frac{1}{2}}\, \hat{\mathbf{h}}_m^+ \cdot \mathbf{H}_{m+1}^- + \psi_{out}^{m-\frac{1}{2}}\, \hat{\mathbf{h}}_m^- \cdot \mathbf{H}_{m-1}^+ - \psi_{in}^{m+\frac{1}{2}}\, \hat{\mathbf{h}}_m^+ \cdot \mathbf{H}_m^+ - \psi_{in}^{m-\frac{1}{2}}\, \hat{\mathbf{h}}_m^- \cdot \mathbf{H}_m^-\right] \quad , \tag{A.13}$$

where $+$, $-$ now denote the right, left inner wall of the cell. We now write, using Eqs. (A.3) and (A.8),

$$Z_0 \mathbf{H}_m^{\pm} = Z_0 \left[I_m \mathbf{h}_m^{\pm} + \hat{I}_m \hat{\mathbf{h}}_m^{\pm}\right] = \frac{jk}{k_m} \mathbf{h}_m^{\pm} V_m + \frac{jk}{\hat{k}_m}\, \hat{\mathbf{h}}_m^{\pm} \hat{V}_m \tag{A.14}$$

and obtain

$$\left[\frac{2 + h_m^2\left(\psi_{in}^+ + \psi_{in}^-\right)}{2k_m^2} - \frac{1}{k^2}\right] V_m = \frac{\psi_{out}^+ h_m h_{m+1}}{2k_m k_{m+1}}\, V_{m+1} + \frac{\psi_{out}^- h_m h_{m-1}}{2k_m k_{m-1}}\, V_{m-1} - \frac{\psi_{out}^+ h_m \hat{h}_{m+1}}{2k_m \hat{k}_{m+1}}\, \hat{V}_{m+1} + \frac{\psi_{out}^- h_m \hat{h}_{m-1}}{2k_m \hat{k}_{m-1}}\, \hat{V}_{m-1} - \frac{\left(\psi_{in}^+ - \psi_{in}^-\right)}{2k_m \hat{k}_m} h_m \hat{h}_m \hat{V}_m \quad , \tag{A.15}$$

$$\left[\frac{2 + \hat{h}_m^2\left(\psi_{in}^+ + \psi_{in}^-\right)}{2\hat{k}_m^2} - \frac{1}{k^2}\right] \hat{V}_m = -\frac{\psi_{out}^+ \hat{h}_m \hat{h}_{m+1}}{2\hat{k}_m \hat{k}_{m+1}}\, \hat{V}_{m+1} - \frac{\psi_{out}^- \hat{h}_m \hat{h}_{m-1}}{2\hat{k}_m \hat{k}_{m-1}}\, \hat{V}_{m-1} + \frac{\psi_{out}^+ \hat{h}_m h_{m+1}}{2\hat{k}_m k_{m+1}}\, V_{m+1} - \frac{\psi_{out}^- \hat{h}_m h_{m-1}}{2\hat{k}_m k_{m-1}}\, V_{m-1} - \frac{\left(\psi_{in}^+ - \psi_{in}^-\right)}{2k_m \hat{k}_m}\, \hat{h}_m h_m V_m \quad . \tag{A.16}$$

We have here included the known symmetry of the TM_{110} and TE_{111} modes, *i.e.*

$$\mathbf{h}_m^+ = \mathbf{h}_m^- \equiv \mathbf{h}_m \quad , \qquad \hat{\mathbf{h}}_m^+ = -\hat{\mathbf{h}}_m^- \equiv \hat{\mathbf{h}}_m \quad , \tag{A.17}$$

and define $h_m = |\mathbf{h}_m|$, $\hat{h}_m = |\hat{\mathbf{h}}_m|$. Eqs. (A.15) and (A.16) correspond to a double circuit chain of resonators. The limitation on these equations comes from the neglect of higher cell modes and from the lowest order static calculation of the coupling constants $\psi_{out}^{\pm}$ and $\psi_{in}^{\pm}$. Note that the system again represents a symmetric eigenvalue problem but now of dimension $2N$, where N is the number of cavity cells.

If we assume the cell variation occurs gradually along the structure then Eqs. (A.15), (A.16) can be written as

$$(x_m-\lambda)f_m-\frac{\kappa_{m+\frac{1}{2}}}{2}f_{m+1}-\frac{\kappa_{m-\frac{1}{2}}}{2}f_{m-1}=-\frac{\sqrt{\kappa_{m+\frac{1}{2}}\hat{\kappa}_{m+\frac{1}{2}}}}{2}\hat{f}_{m+1}+\frac{\sqrt{\kappa_{m-\frac{1}{2}}\hat{\kappa}_{m-\frac{1}{2}}}}{2}\hat{f}_{m-1} \tag{A.18}$$

$$(\hat{x}_m-\lambda)\hat{f}_m+\frac{\hat{\kappa}_{m+\frac{1}{2}}}{2}\hat{f}_{m+1}+\frac{\hat{\kappa}_{m-\frac{1}{2}}}{2}\hat{f}_{m-1}=\frac{\sqrt{\kappa_{m+\frac{1}{2}}\hat{\kappa}_{m+\frac{1}{2}}}}{2}f_{m+1}-\frac{\sqrt{\kappa_{m-\frac{1}{2}}\hat{\kappa}_{m-\frac{1}{2}}}}{2}f_{m-1} \tag{A.19}$$

where we have set $f_m = V_m$, $\hat{f}_m = \hat{V}_m$, $\lambda = \nu^{-2}$,

$$x_m = \frac{1+h_m^2\psi_{in}^m}{\nu_m^2} \quad , \quad \kappa_{m\pm\frac{1}{2}} = \frac{\psi_{out}^{\pm}h_m h_{m\pm1}}{\nu_m\nu_{m\pm1}} \quad , \tag{A.20}$$

$$\hat{x}_m = \frac{1+\hat{h}_m^2\psi_{in}^m}{\hat{\nu}_m^2} \quad , \quad \hat{\kappa}_{m\pm\frac{1}{2}} = \frac{\psi_{out}^{\pm}\hat{h}_m\hat{h}_{m\pm1}}{\hat{\nu}_m\hat{\nu}_{m\pm1}} \quad . \tag{A.21}$$

Note that we have taken, for cell m, $\psi_{in}^+ = \psi_{in}^- \equiv \psi_{in}^m$. As is discussed in the main body of this paper, rather than using Eqs. (A.20), (A.21), to obtain the parameters x_m, $\hat{x}_m$, $\kappa_{m\pm\frac{1}{2}}$, $\hat{\kappa}_{m\pm\frac{1}{2}}$, we will obtain them by fitting to the dispersion curves of periodic structures. Once these parameters are obtained, and the boundary conditions are set, we can solve for the eigenvalues and eigenfunctions of the system.